Nanopatterning of fibronectin and the influence of integrin clustering on endothelial cell spreading and proliferation

John H. Slater, Wolfgang Frey

Department of Biomedical Engineering and Center for Nano and Molecular Science and Technology,
University of Texas at Austin, 1 University Station C0800, Austin, Texas 78712

Abstract: Investigating stages of maturation of cellular adhesions to the extracellular matrix from the initial binding events to the formation of small focal complexes has been challenging because of the difficulty in fabricating the necessary nanopatterned substrates with controlled biochemical functionality. We present the fabrication and characterization of surfaces presenting fibronectin nanopatterns of controlled size and pitch that provide well-defined cellular adhesion sites against a nonadhesive polyethylene glycol background. The nanopatterned surfaces allow us to control the number of fibronectin proteins within each adhesion site from 9 to 250, thereby limiting the number of integrins involved in each cell–substrate adhesion. We demonstrate the presence of fibronectin on the nanoislands, while no protein was observed on the passivated background. We show that the cell adheres to the nanopatterns with adhesions that are much smaller and more evenly distributed than on a glass control. The nanopattern influences cellular proliferation only at longer times, but influences spreading at both early and later times, indicating adhesion size and adhesion density play a role in controlling cell adhesion and signaling. However, the overall density of fibronectin on all patterns is far lower than on homogeneously coated control surfaces, showing that the local density of adhesion ligands, not the average density, is the important parameter for cell proliferation and spreading. © 2007 Wiley Periodicals, Inc. J Biomed Mater Res 87A: 176–195, 2008

Key words: endothelial cell; nanopattern; fibronectin; focal adhesion; integrin

INTRODUCTION

Integrins mediate cellular interactions with the underlying extracellular matrix (ECM) and form adhesion sites that are key regulators of intracellular signaling cascades that govern many aspects of cellular behavior.[1–5] Although individual integrins, activated by ligand binding or conformational changes alone, can form stable adhesions, it is the clustering of ligated integrins that induces many of the signaling events, and which is necessary for strong interactions with actin fibers.[6–9] By contrast, clustering of nonligated integrins accumulate a large number of signaling molecules, but fail to engage the actin cytoskeleton.[7] Groups of only three integrins, activated by ligand binding, are needed to form an activated cluster,[8] although these clusters immediately form larger structures that then link to the cytoskeleton. Activated and clustered integrins therefore act synergistically and recruit a large variety of scaffold and signaling molecules with spatial and temporal dependence, leading to the formation of focal complexes that mature into focal adhesions.[10–13]

Focal complexes and focal adhesions regulate motility,[14–17] proliferation,[2,18–20] differentiation,[18,20] and apoptosis.[21,22] While often biochemical in nature, these regulatory processes are also determined by the endogenous force generated by the cell with its actomyosin network through the adhesion complexes on the substrate.[23–25] Adhesions have been shown to support forces proportional to the adhesion size, except for small adhesions mostly at the protruding edge of motile cells, which show higher forces with little or inverse proportionality to size.[26–28] Consequently, the substrate compliance and the density of integrin ligands play important roles in cell motility, leading to a biphasic dependence of the motility on the ligand density and the elastic modulus.[29–31] Changes in substrate compliance and ligand density also lead to an altered distribution of focal

adhesions and variations in adhesion size.[24,30] The exact mechanism of the integrin-mediated mechanotransduction process is still unclear, and tools that allow a systematic variation of the size of individual clusters may lead to a better understanding of the forces exerted in each cluster as well as of the molecular processes that drive the maturation process of cellular adhesions.

ECM protein or ECM fragment-coated micro- and nanobeads have been a very successful technique to explore the minimum size of a ligand cluster,[8] the force exerted on these small clusters,[32] the locality of the response to ligand binding,[33] and the dynamics and directionality of integrin movement.[34,35] However, only larger surfaces that present ECM proteins in a controlled density or pattern can systematically explore parameters such as a larger range of forces, the maturation process of adhesions, and the processes associated with cell motility.

Direct control over focal adhesion dimensions can only be achieved with surfaces that present precise nanometer-sized adhesion areas surrounded by a nonadhesive background. Micropatterned functional surfaces are easily achieved using microcontact printing[36,37] or traditional lithography techniques,[38–40] and these have been successfully used to show the influence of spreading area and geometry on cell proliferation, differentiation, and signaling.[37,41,42] It is still a challenge, however, to produce nanopatterned dual-functional surfaces that are large enough for statistical cell studies. For controlled chemical functionality at the nanometer scale, these fabrication processes have to create surface nanopatterns of ECM components, either full proteins or peptide sequences adsorbed or covalently linked to the surface in nanometer-sized patches surrounded by a passive background that does not support protein adsorption or cellular attachment. Because of these conditions, only a few nanopatterning strategies exist that can provide defined nanoislands of cell adhesion molecules,[43–48] and even fewer have been used for systematic studies of cellular adhesion and motility.[43,46,47,49]

Clustering of integrins to within about 60 nm of each other is necessary for long-term cell attachment and focal adhesion formation using micelle nanolithography.[43] This integrin spacing corresponds to the typical range of sizes and repeats found in key adhesion molecules such as fibronectin, collagen, and talin. Also, adhesion strength is increased and cells show higher motility on small clusters of RGD peptides compared with equivalent densities of homogeneous distribution, although only statistical averages of cluster distances could be controlled.[46–48]

The idea that the local density of ligands is more important than the overall density has been suggested by analyzing morphological parameters of cells seeded on fibronectin (FN) islands down to a size of 0.1 μm^2 with varying island separation created using microcontact printing.[50] However, no experimental investigations exist that analyze the range of cluster sizes from 40 to 300 nm, corresponding to about 9–250 fibronectins per island. This size range could be key to understanding the importance of the immediate aggregation seen with ligand trimers,[8] the different levels of integrin activation found at early adhesions,[51] and the early processes in the maturation of focal complexes into adhesions during motility[52] and spreading.[53] One would therefore also expect adhesions restricted to the size range of 40–300 nm to allow for an important range of forces per adhesion cluster and the impact on cell adhesion, cytoskeletal development, and cell motility to be investigated.

Here we introduce a patterning technique based on nanosphere lithography (NSL),[54,55] which has been used as a template for the fabrication of protein[56] or chemical arrays, but is here expanded to use orthogonal functionalization to tightly control the cells' ability to build adhesions. Our technique produces large areas (cm^2) of nanoislands whose size and spacing is controlled by the sphere diameter and by monolayer or bilayer mask configurations.[55,57] We create FN islands surrounded by poly (ethylene glycol) (PEG) passivated areas, which, instead of using RGD-containing peptides, allows us to utilize the stronger binding to the full-length protein that includes, for instance, the synergistic binding site. Because the goal is to present well-defined adhesion sites, we characterized the surfaces using X-ray photoelectron spectroscopy (XPS), atomic force microscopy (AFM), and cell-seeding studies to show that FN adsorbs specifically to the nanopatterned islands but not to the PEG-treated background. We present initial characterizations of cell adhesion, spreading, and proliferation to show the influence of adhesion site size, and to introduce an experimental platform that can be used for future cell motility and signaling studies.

MATERIALS AND METHODS

Nanopattern fabrication

Plain microscope glass slides (Erie Scientific Company, Portsmouth, NH) were cleaned in piranha solution (H_2SO_4:H_2O_2 3:1) (Fisher Scientific, Pittsburgh, PA) for 20 min at 85°C. The slides were thoroughly rinsed with distilled deionized (DI) water (Barnstead International, Dubuque, IA) to remove residual acid. NSL was used to create the nanopatterns. Briefly, polystyrene spheres (PS) (Duke Scientific, Fremont, CA) of a chosen diameter were dialyzed, using a 10,000-MW cut-off membrane, (Pierce Biotechnology, Rockford, IL) following the sphere manu-

facturer's instructions to remove unwanted surfactants and then deposited in either a monolayer or bilayer configuration onto a clean glass surface using a custom-built capillary deposition machine similar to that in Refs. 58 and 59. Two nanometers of chromium (Cr) (R.D. Mathis, Long Beach, CA) and 8 nm of gold (Au) (Alfa Aesar, Ward Hill, MA) were thermally evaporated onto the surface (Denton Vacuum, Moorestown, NJ). The spheres were removed by sonication in methanol and the resulting nanopatterned surface was immediately functionalized for cell adhesion experiments.

Nanopattern imaging and characterization

AFM images were acquired using an MFP-3D AFM (Asylum Research, Santa Barbara, CA). Standard silicon cantilevers, AC240TS (72 kHz, Olympus Optical, Japan) were used for alternating current mode imaging, and nonconducting silicon nitride sharpened cantilevers (Veeco Metrology, Santa Barbara, CA) were used for contact mode imaging. Image processing, analysis, and 3D enhancement were performed using MFP-3D software in Igor Pro 5 (WaveMetrics, Lake Oswego, OR) and with ImageJ (NIH, Bethesda, MD). The individual island size, island areas, island-to-island spacing, topography, and percent surface coverage were measured from the AFM images without performing tip deconvolution.

Dual chemical functionalization

Nanopatterned glass slides were exposed to an air plasma at 300 µTorr at ~50 W for 10 min (March Instruments, Concord, CA). The nanopatterned slides were then immersed in a 26.5 mM hydrochloric acid (Fisher Scientific, Pittsburgh, PA), 1 mM hexadecane thiol (Aldrich, St. Louis, MO), and 41 mM 2-methoxy(polyethyleneoxy)–propyltrimethoxysilane (PEG-silane) (Gelest, Morrisville, PA) solution in toluene (Fisher Scientific, Pittsburgh, PA) in a self-standing centrifuge tube (Corning, Corning, NY) for 48 h with continuous stirring, adapted and extended from Ref. 60. The samples were vigorously rinsed once in toluene and twice in ethanol, dried with nitrogen, and baked at 105°C for 1 h. The chemically functionalized patterned surfaces were exposed to 3 mL of bovine plasma fibronectin or human plasma fibronectin (Sigma, Saint Louis, MO) solution at a concentration of 10 µg/mL in 50 mM HEPES for 20 min, followed by two thorough rinses in HEPES solution to remove excess fibronectin. Cells were seeded immediately following FN adsorption.

Analysis of surface modification

A PHI 5700 XPS system (Physical Electronics, Chanhassen, MN) equipped with a dual Mg and monochromatic Al X-ray source was used at a fixed angle of 45° for elemental analysis of the chemically modified surfaces. The surfaces were survey scanned to determine the elemental composition percentages for Si_{2p}, C_{1s}, N_{1s}, Au_{4f}, and O_{1s} on each surface and S_{2p} on some. High-resolution scans with a dwell time of 500 ms and with a pass energy of

58.7 eV were used to acquire the Au_{4f}, N_{1s}, S_{2p}, and Si_{2p} spectra and a pass energy of 11.75 eV was used for the C_{1s} spectra with charge correction set to 285 eV for nonconducting samples. Three distinct areas were measured and averaged for each sample. PeakFit software (Systat Software, Point Richmond, CA) and a multipeak fit package in Igor Pro 5 (WaveMetrics, Lake Oswego, OR) were used to fit the high resolution C_{1s} scans with multiple Gaussian curves and linear baseline correction to analyze the bond types present within each peak. Nine different surface types were examined: (1) a dual functionalized gold surface, (2) a dual functionalized gold surface with FN adsorbed at concentrations of 2, 5, 10, 25, and 50 µg/mL, (3) a dual functionalized glass surface, (4) a dual functionalized glass surface with adsorbed FN, (5) a plain glass surface with adsorbed FN at concentrations of 2, 5, 10, 25, and 50 µg/mL, and (6) 0400M, (7) 0400B, (8) 0300B, and (9) 0300M surfaces that were functionalized and exposed to FN at a concentration of 10 µg/mL (see Table I for nanopattern descriptions). It should be noted that even pure gold or glass surfaces were treated with the full chemistry, thiol and silane, to insure that no nonspecific interactions took place on the surfaces.

Cells and reagents

Pooled and nonpooled human umbilical vein endothelial cells (HUVECs), passages 2–4, were cultured in endothelial growth media (EGM) supplemented with 2 mL of bovine brain extract, 0.5 mL of human endothelial growth factor, 0.5 mL of hydrocortisone, 0.5 mL of gentamicin/amphotericin-B, and 10 mL of fetal bovine serum according to manufacturer's instructions (all reagents and cells: Cambrex Bio Science Walkersville, Walkersville, MD). The cells were grown to 90% confluence in T-25 tissue culture flasks that were coated with 30 µg of bovine or human plasma fibronectin (Sigma, Saint Louis, MO) at 37°C and 5% CO_2. Before seeding onto sample slides, the cells were trypsinized with 3.0 mL of 0.25% trypsin and 1 mM ethylenediaminetetraacetic acid in PBS at 37°C for 5 min. The cells were collected and centrifuged at 240g for 10 min. The cell pellet was then resuspended in full EGM media and seeded onto the desired substrate at a density of ~40 cells/mm^2.

Fibronectin adsorption analysis

Nanopatterned samples functionalized with fibronectin were analyzed before and after cell seeding. After fibronectin adsorption, following a procedure modified from ref. 61, the nanopatterned surfaces were incubated in 1 mM bis (sulfosuccinimidyl)suberate (BS^3) (Pierce, Rockland, IL), a water-soluble, noncleavable, and membrane-impermeable crosslinker, at 20°C for 10 min. Unreacted crosslinker was quenched with 20 mM glycine in PBS. Samples that had been seeded with cells were treated similarly, with the addition of a cell removal step using 0.2% SDS (sodiumdodecylsulfate) in PBS for 10 min after crosslinking. Each surface was finally washed three times with PBS and imaged with AFM as described earlier.

TABLE I
Nomenclature, Pattern Size, Pitch, and Pattern Area for the Nanopatterned Surfaces Used

Pattern Name	Sphere Diameter (nm)	Characteristic Length (nm)	Center-to-Center Spacing [Rim-to-Rim Spacing] (nm)	Island Area (nm^2)
1500M	1500	405 ± 41	883 ± 51 [478]	85,653 ± 17,044
1000M	1000	305 ± 39	589 ± 27 [284]	55,923 ± 7273
0820M	820	255 ± 24	470 ± 22 [215]	37,049 ± 4974
0500M	500	157 ± 19	285 ± 16 [128]	14,947 ± 2778
0400M/0420M	400/420	97 ± 9	253 ± 13 [156]	6485 ± 686
0400B/0420B	400/420	102 ± 16	414 ± 12 [312]	4675 ± 2481
0300M	300	94 ± 11	177 ± 13 [83]	5191 ± 1298
0300B	300	92 ± 33	308 ± 11 [216]	3629 ± 1013

M, monolayer mask; B, bilayer mask. The characteristic length refers to the length of the longest bisector of the triangular pattern, the center-to-center spacing (pitch) is measured from the center of one nanoisland to the center of its nearest neighbor, and the rim-to-rim spacing from the rim of one nanoisland to the closest rim of its nearest neighbor. All measurements were made from multiple high resolution AFM scans ($n \geq 100$, error = 1 SD).

Dual fluorescent-atomic force adhesion site imaging

After 72 h of incubation, the samples were rinsed twice with PBS followed by fixation in 5% formaldehyde in PBS for 20 min at 37°C. The samples were rinsed with PBS and blocked with 1.0% BSA solution in PBS for 20 min and rinsed twice with PBS. Samples were then incubated in a vinculin stain solution (1% by volume of FITC-conjugated mouse anti-vinculin in 1.0% BSA and 0.01% Tween 20 in PBS) (all Sigma, Saint Louis, MO) overnight at 4°C. The samples were rinsed twice with PBS supplemented with 0.01% Tween 20 and rocked in PBS with 0.1% Tween 20 for 20 min followed by a DI H$_2$O rinse and nitrogen drying. Fluorescent images were acquired using an Olympus IX70 inverted microscope equipped with an X-100 CCD camera with InstaGater on-chip integration (Dage-MTI, Michigan City, IN) connected to an MFP-3D AFM (Asylum Research, Santa Barbara, CA). AFM images were collected over the fluorescently imaged areas as described earlier. The vinculin-containing adhesions in the AFM images were identified by matching the location to that observed in the simultaneous fluorescent images and by their increased height above the background. Height traces were drawn and the adhesion heights measured using MFP-3D software in Igor Pro 5 (WaveMetrics, Lake Oswego, OR). For the two cells shown in Figure 5 each adhesion site's length (dash adhesions) or diameter (dot adhesions) and area were determined from the AFM scans using ImageJ (NIH, Bethesda, MD).

Cell proliferation and cell spreading area studies

HUVECs were sparsely seeded at ~40 cells/mm^2. Twenty 15× magnification phase contrast images were collected 4 h after initial seeding and at 24-h time intervals for 3 days for each sample. Additionally, fifty 40× magnification phase contrast images were collected every 24 h for 3 days. Cell densities (number of cells per surface area) were measured over a 21 mm^2 area. Cell proliferation rates were calculated after normalizing the cell densities at each time point to its initial average seeding density at 4 h and a heteroscedastic t test assuming unequal variance was used to determine significant differences in the normalized data. Cell proliferation assays, such as BrdU DNA synthesis assays or fluorescent-activated cell sorting (FACS), are a more specific proliferation test, but could lead to misleading results due to incomplete nanopattern coverage in some areas of the sample. The cell spreading areas for a minimum of 100 cells were measured by hand on a Motion Computing LE1600 Tablet PC (Motion Computing, Austin, TX) using the outline feature in ImageJ (NIH, Bethesda, MD). To separate surface effects from other stimuli, only cells that had just one nucleus and were not in intimate contact with neighboring cells were analyzed for the cell spreading area study. Statistical analysis was performed using SPSS 12.0 (SPSS, Chicago, IL). ANOVA with post hoc Tukey and Bonferroni tests and nonparametric Kruskal–Wallis with a post hoc Dunn procedure were both applied to compare the measured projected cell spreading areas.

RESULTS

Nanopattern fabrication and functionalization

The NSL fabrication process allows us to fabricate patterns with characteristic lengths ranging from 90 to 400 nm with homogenous topography of 10–13 nm over cm^2 areas. Figure 1(A) schematically outlines the process used to create the surfaces. First, a monolayer or bilayer of densely packed nanospheres is deposited onto the surface with a custom-built deposition machine [Fig. 1(B)]. A 2-nm adhesion layer of chromium and an 8-nm layer of gold are then thermally evaporated onto the surface, followed by sphere removal using sonication in methanol. This leaves an array of truncated triangular pyramids of gold in a hexagonal or orthorhombic lattice surrounded by glass [Fig. 1(C,D)].

The resulting surface is composed of two materials that allow for two separate functionalization chemistries to be applied, such as thiols for the gold and
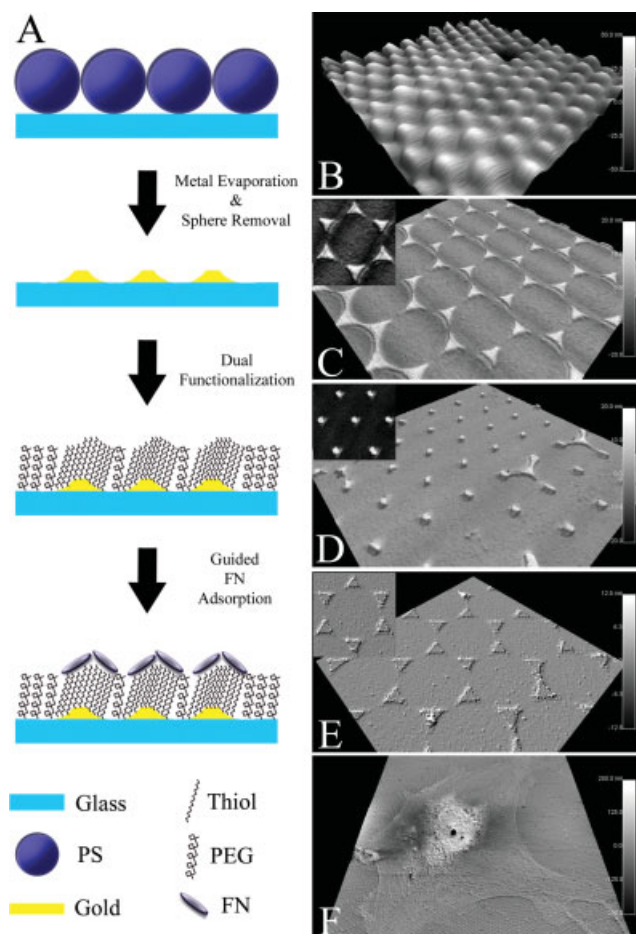
Figure 1. (A) Schematic depicting the nanopattern fabrication process, chemical functionalization, and directed fibronectin adsorption to the chemically modified nanopatterns. 3D AFM images with zoomed-in inserts of (B) monolayer mask of 500-nm diameter spheres (scan size 5 μm × 5 μm) (C) 0420M surface (scan size 2 μm × 2 μm) (D) 1500B surface (scan size 10 μm × 10 μm) (E) 1500M surface after dual chemical functionalization and fibronectin adsorption (scan size 5 μm × 5 μm) and (F) HUVEC seeded on a 0300M surface after the full surface treatment (scan size 90 μm × 90 μm). [Color figure can be viewed in the online issue, which is available at www.interscience.wiley.com.]

silanes for the glass areas. After sphere removal the surface is exposed to the O_2 plasma to produce hydroxyl groups on the glass surface. The hydroxyls are necessary to create a high density of coupling sites for the silane selfassembled monolayer (SAM). Low-density PEG-SAMs are not effective in preventing protein adsorption and subsequent cellular attachment. For dual SAM functionalization, the freshly oxidized surface is immersed in a solution containing the hexadecane thiol and the PEG-silane for 48 h. Since the oxygen plasma treatment would destroy the thiol molecules, and with the tendency of the silane to nonspecifically adsorb to the gold if no thiol is present, the thiol and silane surface function-

alizations are performed simultaneously. The combination of solvents does not mix completely, and thus must be stirred vigorously. Shorter incubation times and different concentrations of PEG-silane in the mixture led to increased cell adhesion to the PEG-surfaces (see Cell Seeding on Functionalized ½ Au–½ Glass Surfaces). The SAM-functionalized surface is then exposed to a FN solution, where FN is only able to adsorb to the gold nanopatterns producing FN nanoislands of controlled size and pitch surrounded by a nonadhesive background [see the changed texture of the pattern in Fig. 1(E) compared with 1(C)]. Finally, cells are seeded onto the surface [Fig. 1(F)].

Table I summarizes the samples used, named according to the size (in nm) of the spheres used and the type of mask, monolayer (M) and bilayer (B). The table also lists the measured sizes, the bisector of the triangle for monolayer (M) or the diameter of the dots for bilayer (B) samples, the distances between the nanoislands, and the projected areas as a function of the sphere diameter and mask type. The measured dimensions of the nanoislands ranged from 12 to 25% larger than the calculated theoretical sizes, yet the island-to-island spacing was within 2% of the theoretical values.[55,57] This could be attributed to inhomogeneities in the sphere size, nonperpendicular metal evaporation, or to convolution effects from the AFM tips. The measured percent surface coverage of the nanoislands was 7.2% ± 0.4% and 2.3% ± 0.4%, for mono- and bilayers, respectively, and closely matched the calculated theoretical values of 7.2 and 2.2%.

Surface characterization with XPS

XPS was used to confirm that the surface chemistry is selective, even on the nanometer scale, and that FN adsorbs exclusively to the methylated gold areas while leaving the passivated PEG-glass background free of protein, and to determine the FN surface concentrations after adsorption. The analysis was performed before chemical treatment, after simultaneous functionalization with thiol and silane, and after FN adsorption. Four nanopatterned surfaces, 0300B, 0300M, 0400M, and 0400B, were analyzed after the full modification protocol.

The results from the XPS elemental analysis for the simultaneous functionalization with thiol and silane SAMs are given in Table II (for the spectral analysis see supplemental data). Several indicators have been used to confirm protein adsorption by XPS analysis[62–64]: the appearance of a distinct N_{1s} peak indicating the presence of nitrogen in protein, an increase in the C—N, C—C, C—O, and N—C=O bond contributions to the C_{1s} spectra from FN, and a

Surface	Au_{4f}	Si_{2p}	S_{2p}	O_{1s}	N_{1s}	C_{1s}
Glass-PEG-Thiol	0.01	20.84	0.00	60.39	0.14	18.63
Glass-PEG-Thiol-10 µg/mL FN	0.01	17.68	0.00	57.97	0.27	24.06
Au-Thiol-PEG	15.43	0.00	3.13	46.85	0.51	34.08
Au-Thiol-PEG-1,882 FN/µm^2	10.93	2.31	1.15	31.33	4.27	50.01
0400B-Thoil-PEG- 41 FN/µm^2	0.20	19.72	ND	49.08	0.75	30.25
0400M-Thiol-PEG- 217 FN/µm^2	0.77	20.28	ND	49.87	0.81	28.26

ND, not determined.

decrease in the background (Au_{4f}, Si_{2p}) signal as the protein shadows the substrate signal.

We used the most direct and specific indicator for protein adsorption, the appearance of a nitrogen N_{1s} peak, which is absent in all samples before FN absorption. While a clear N_{1s} peak was observed after protein adsorption on the modified gold [Fig. 2(F)] and plain glass surfaces [Fig. 2(E)], no distinct N_{1s} peak was seen on PEGylated glass samples either before or after FN adsorption [Fig. 2(D)]. To quantify the adsorption of FN, we established a calibration relation of the Gaussian-fit area under the N_{1s} peak at different concentrations of FN in solution. The typical sigmoidal behavior that has been observed with ^{125}I-labeled FN[61] is reproduced with the N_{1s} area measurements [Fig. 2(A)]. A quantification of the amount of FN can be achieved by fitting the data to a sigmoidal curve and comparing the saturation value of the XPS signal of FN on thiolated gold surfaces to published data of ^{125}I-labeled FN adsorbed to CH$_3$-terminated silane SAMs,[61] which is very similar to adsorption curves found for tissue culture polystyrene and glass.[65] We also examined the background signal to quantify the extent of shadowing as FN is adsorbed to the surfaces. The background signals for both, Au_{4f} for gold and Si_{2p} for glass, exponentially decrease as the FN density increases [Fig. 2(B,C)].

A FN saturation value of 190 ng/cm^2 (2543 FN molecules per square µm) occurred on CH$_3$-terminated silane SAMs when exposed to a 20 µg/mL solution of FN.[61] The calibration curves indicate that a monolayer of FN is formed on clean glass at a surface concentration of 2300 FN/µm^2. The saturation value for a thiolated gold surface is slightly higher at 2605 FN/µm^2. The higher saturation value is attributed to the fact that FN has a more compact form when adsorbed to hydrophobic surfaces thereby inducing a higher packing density for a monolayer of protein on thiolated gold than would be expected on a glass surface.[66] Furthermore, we were able to show that the mono- and bilayer nanopatterned surfaces, respectively, adsorb 8.3% (217 FN/µm^2) and 1.6% (41 FN/µm^2) of the amount of protein as the nonpatterned thiolated gold surfaces. These values are close to the measured pattern surface coverage of 7.2 and 2.3% for the mono- and bilayer surfaces, respectively, indicating that the FN adsorbs almost exclusively to the thiolated gold nanopatterns and avoids the passive PEG background.

We deconvoluted the C_{1s} signal for contributions from chemical bond energies that are expected in the PEG, thiol, and FN chemical structures. The C_{1s} spectra for the functionalized and protein-treated homogenous gold and plain glass samples were fit with three Gaussian curves corresponding to the expected bond energies of the C—C (285.0 eV), C—N (286.0 eV), C—O and PEO (286.5 eV), and N—C=O (288.3 eV) bonds.[67] Previous XPS studies on proteins, including FN, have shown that it is difficult to differentiate the C—O and C—N peaks from one another and that they can be fit as a single peak centered in the range of 285.7–286.5 eV.[68] In our data, the peak position occurred in this same range, usually centered at 286.5 eV. The relative contribution of each bond to the total C_{1s} energy for the gold and nanopatterned surfaces is displayed in Table III; glass data are not shown due to their similarity to the gold surfaces.

After protein adsorption, the appearance of a nitrogen N_{1s} peak on the gold sample is accompanied by the appearance of two additional peaks in the C_{1s} spectra at 286.5 and 288.3 eV, which indicate the presence of amine, ether, and amide bonds [Fig. 2(F)], similar to previous results.[68,69] The characteristic protein peak contributions to the C_{1s} spectra consisted of 64.5% C—C bonds from the thiol and the FN backbone, 23.4% C—N and C—O bonds, and 12.0% N—C=O bonds for the gold surface with a FN density of 1882 FN/µm^2. The C—C contribution to the C_{1s} spectra decreases and the C—N, C—O, and N—C=O contributions increase as more protein is added to the thiolated gold surfaces (Table III). The PEG-silane functionalized glass samples show the expected C—C and PEG peaks, but no amide bond peak [Fig. 2(D)] after FN adsorption. A ratio of C—C to PEG components of about 1:4 would be expected, but the contribution of the C—C peak is larger [Fig. 2(D)]. We attribute this to a small amount of hydrocarbon contamination or possibly to some thiols
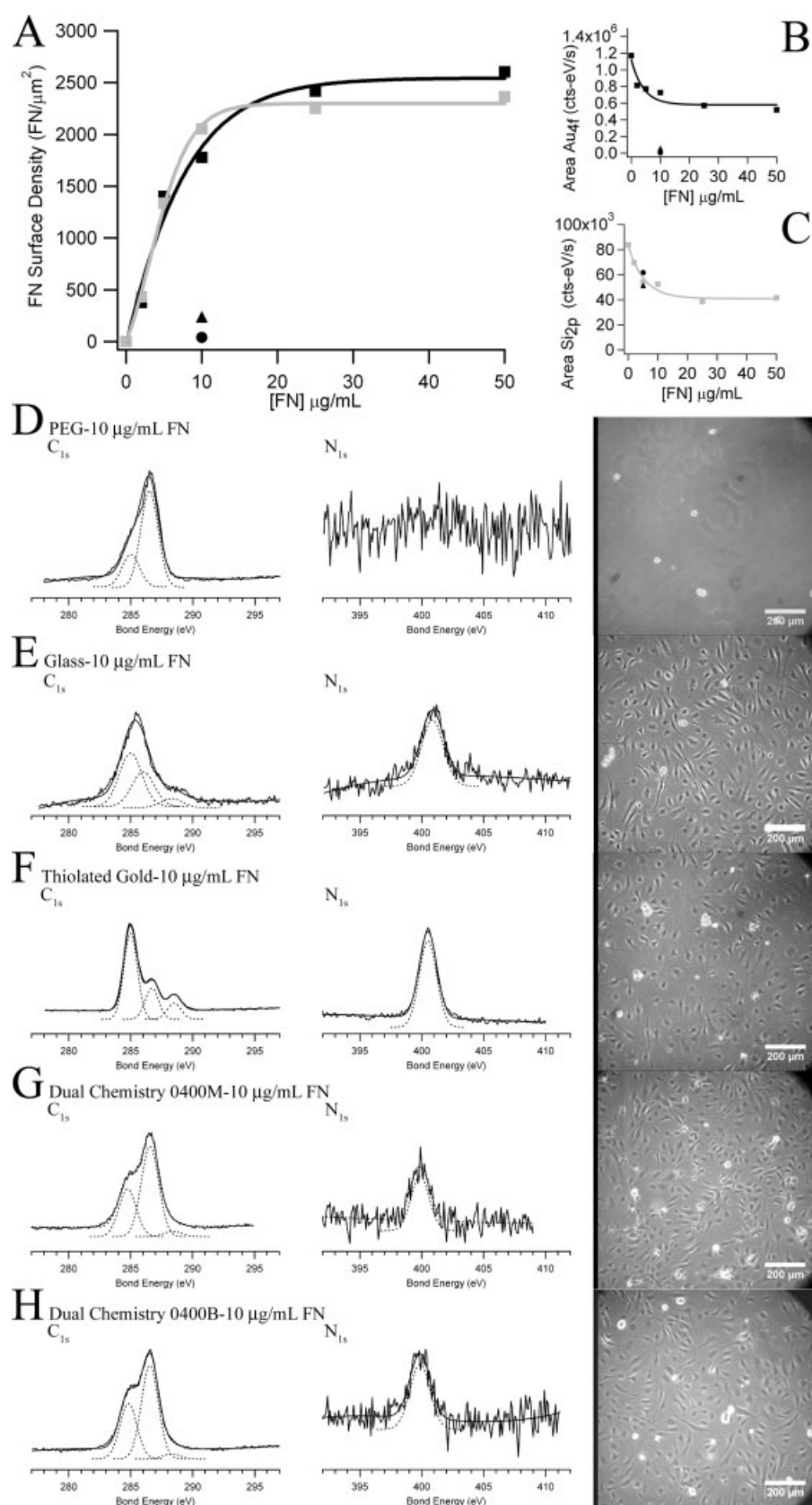
Figure 2.

TABLE III
Deconvolution of the XPS C_{1s} Peak into the Chemical Bond Energies for Each Test Sample (in % of total peak area)

Surface	C—C 285.0 eV	C—N, C—O, PEO 285.7–286.5 eV	N—C=O 288.3 eV
Glass-PEG-Thiol	32.93	67.07	–
Glass-PEG-Thiol-10 µg/mL FN	25.16	74.84	–
Au-Thiol-PEG	92.88	7.12	–
Au-Thiol-PEG-537 FN/µm^2	81.79	13.53	4.68
Au-Thiol-PEG-1,199 FN/µm^2	64.35	24.58	11.06
Au-Thiol-PEG-1,882 FN/µm^2	64.54	23.42	12.04
Au-Thiol-PEG-2,474 FN/µm^2	56.87	26.29	16.84
Au-Thiol-PEG-2,605 FN/µm^2	55.55	27.39	17.70
0400B-Thoil-PEG- 41 FN/µm^2	35.88	60.69	3.43
0400M-Thiol-PEG- 217 FN/µm^2	33.35	63.01	3.65

The appearance of C—N and N—C=O bonds was observed after the addition of FN to the modified gold surfaces. A small N—C=O peak was also detected on both nanopatterned surfaces and was not observed after FN adsorption to the PEG-functionalized glass surfaces.

entrapped in the PEG layer, although no sulfur was detected. Still, the absence of a 288.3 eV amide bond peak and a nitrogen N_{1s} peak on the PEGylated surface indicate a protein-repulsive surface.

On the four nanopatterned surfaces, two small N_{1s} peaks appeared after functionalizing with thiol/silane and FN [Fig. 2(G,H)]. Data for 0300M and 0300B are very similar to the 0400M and 0400B surfaces, respectively (not shown). An evaluation of the C_{1s} curve shows that both nanopatterned surfaces have a noticeable N—C=O signature that is not present on the PEG-functionalized glass, which, together with the appearance of an N_{1s} peak, indicates FN adsorption as seen on the functionalized nonpatterned gold surfaces. A comparison of the area under the N_{1s} curves of the nanopatterned surfaces to the nonpatterned gold surfaces after FN adsorption shows that the amount of protein surface coverage (8.3% for M and 1.6% for B surfaces) on the nanopatterns is close to the measured nanopattern surface coverage (7.2% for the M and 2.3% for the B samples). Also, the area under the amide bond peak at 288.3 eV for the monolayer nanopatterned surfaces is 7% of the area for the same portion of the C_{1s} spectra of the protein-adsorbed gold sample.

The gold background on the monolayer nanopatterned surfaces displayed 8.9% the amount of gold compared with the nonpatterned controls, in good agreement with the measured 8.3% surface coverage of FN. As expected, the nanopatterned surfaces had higher signals from the Si_{2p} spectra, indicating that no protein was adsorbed to the functionalized glass background.

Taken together, these results indicate selective binding of the silane and thiol functionalities to the glass and gold areas, respectively, and selective FN adsorption to the thiolated gold areas. The presence of signatures for the thiol and PEG and distinct N_{1s} peaks on the protein-adsorbed gold, unmodified glass surface, and on nanopatterned surfaces that are absent on the PEGylated glass sample indicate that the chemical functionality can be translated to the nanometer scale and FN can be adsorbed to very small thiolated gold nanoislands. This precise placement of chemical functionality and subsequent protein adsorption is the basis for control of the adhesion site dimensions that are designed to influence cell behavior in contact with the biomaterial surface.

Cell seeding on functionalized ½ Au–½ glass surfaces

To validate the XPS data, HUVECs were seeded on the modified surfaces. Time-dependent functional

Figure 2. (A) Calibration curves depicting the surface density of FN (FN/µm^2) on (□-grey) clean glass and (■-black) functionalized gold surfaces as a function of the solution concentration. The surface density of FN is also shown for both (▲) M and (●) B nanopatterned surfaces. Calibration curves showing the exponential decay of the background signal (Au$_{4f}$ for gold and Si$_{2p}$ for glass) as protein is adsorbed at higher concentrations for functionalized (B) gold and (C) clean glass surfaces, (▲) M and (●) B show values for the nanopatterned surfaces. (D-H) XPS data comparing C_{1s} and N_{1s} spectra for nonpatterned and nanopatterned surfaces after dual functionalization and FN adsorption (10 µg/mL), and phase contrast images of cells seeded on the respective surfaces. (D) PEGylated glass surface, (E) unmodified glass, (F) thiolated gold, (G) 0400M, and (H) 0400B surfaces. The FN contribution to the C_{1s} spectra (C—C, C—N, N—C=O) is shown for the (E) glass, (F) gold, (G) 0400M, and (H) 0400B surfaces and the N—C=O is not seen on the (D) PEGylated glass. The characteristic N_{1s} peak corresponding to adsorbed FN is detected on the (E) untreated glass sample, (F) gold, (G) 0400M, and (H) 0400B surfaces and not on the (D) PEGylated glass. Cells adhered to, spread, and proliferated on the (E) unmodified glass, (F) gold, (G) 0400M, and (H) 0400B surfaces over 3 days whereas almost no cells attached to the (D) PEGylated glass surface.
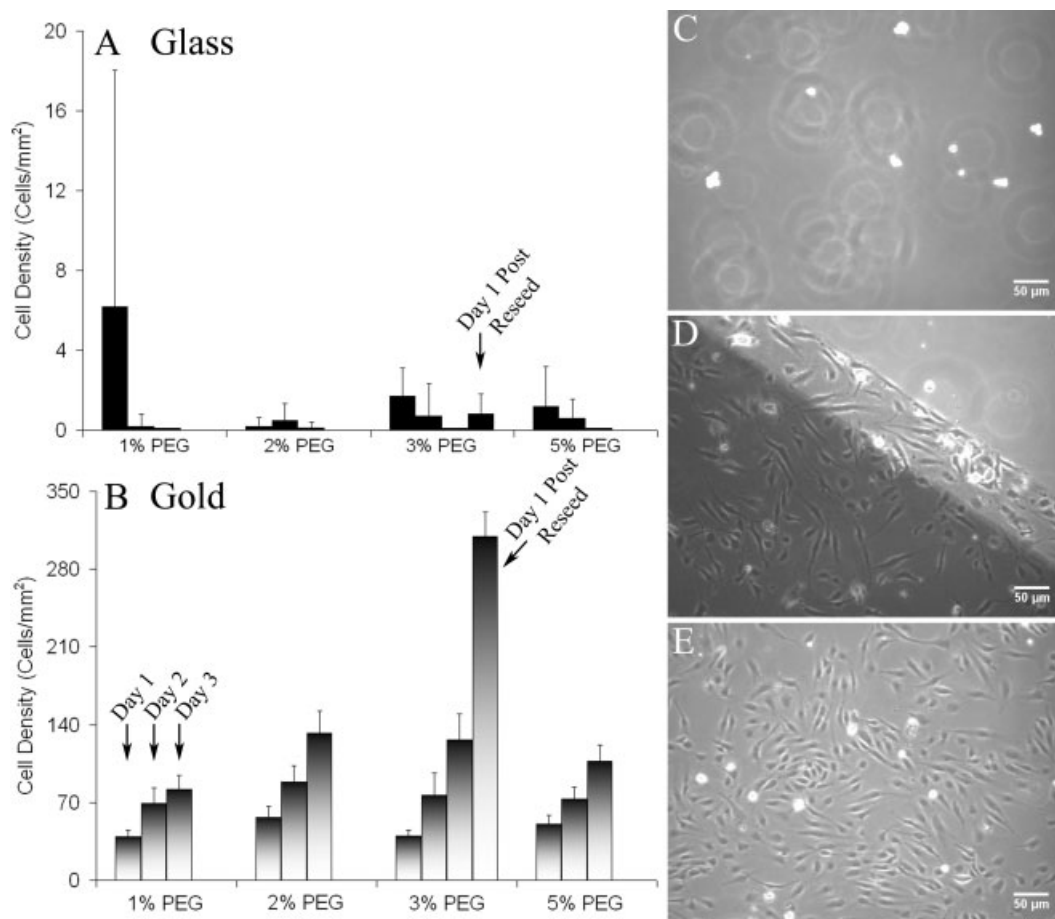
Figure 3. Number of cells per surface area for HUVECs seeded on ½ Au–½ glass slides after chemical functionalization and FN adsorption. (A) Density of adherent cells on the PEG-treated glass half, and (B) on the functionalized gold half measured at 24-h intervals. The fourth bar on the 3% PEG sample shows the cell density 24 h after reseeding cells at Day 3 to test the stability of the chemical pattern contrast. (C–E) Phase contrast images of HUVECs on the ½Au–½glass slides after 3 days in culture. (D) HUVECs grow on and align with the gold-glass intersection. Representative images of cell density on Au half (E) and glass half (C) after 3 days ($n = 20$, error bars = 1 SD).

controls to show that the surfaces selectively support cell adhesion and repulsion on the functionalized gold and glass areas, respectively, were performed on ½Au–½glass slides. Slides underwent full chemical functionalization treatment as described above, but with varying concentrations of PEG-silane (1, 2, 3, and 5% by volume) before seeding with HUVECs. Cells adhered to and proliferated on all of the surfaces [Fig. 3(B,E)] except for the PEG-silane functionalized glass surface [Fig. 3(A,C)], again reaffirming that the PEG layer prevents protein adsorption to the glass areas and consequently inhibits cell attachment. Figure 3(D) shows a phase-contrast image of the intersection of the gold and glass halves after 3 days of culture. The HUVECs have grown to near confluence on the gold half and align to the boundary. A small strip of cells can be seen protruding into the lighter glass side, probably caused by imperfect shadowing of the deposition mask allowing a small amount of gold to deposit in the transition zone. The density of adhered cells increased on the

gold-coated side over 3 days for all four silane concentrations, while very few cells adhered to the PEG-treated glass side. However, the density of cells was the lowest on the 2% PEG-silane surfaces, which we therefore used as our standard concentration for all subsequent experiments.

In addition to the initial ability of the PEG surfaces to reject cell adhesion, we tested whether ECM adsorption from the serum-containing media could support cell attachment. After 3 days of culture in serum-containing media the ½Au–½glass surfaces (3% PEG) were reseeded with four times the number of cells used for the original seeding. On the fourth day, 24 h after the samples had been seeded again, a large spike in cell density was observed on the gold half, while almost no cells were seen on the PEG-functionalized glass half [Fig. 3(A,B)]. This indicates that the PEG-functionalized glass retained its passivating properties against protein adsorption and subsequent cellular attachment for at least 4 days in serum-containing media.
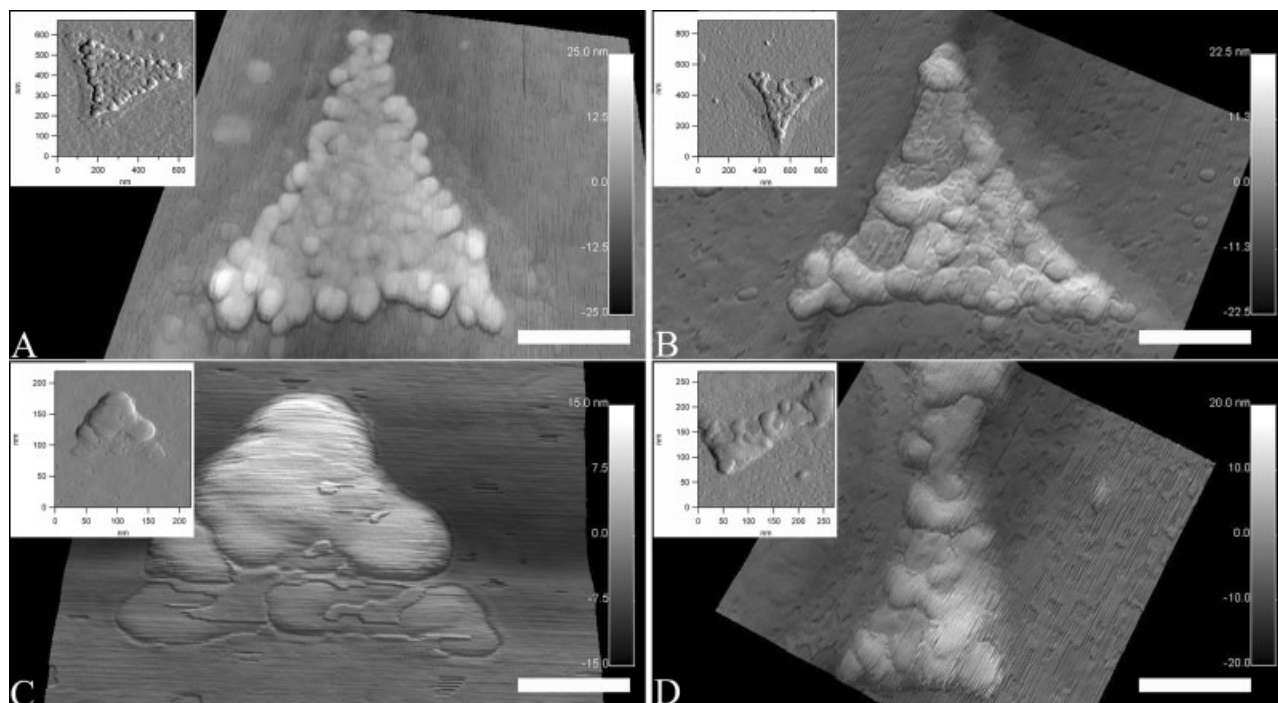
Figure 4. The 3D images from AFM scans (inserts) displaying crosslinked FN on a nanoisland. FN on a 1500M surface before (A) and after (B) cell attachment, and FN on a 0420M surface before (C) and after (D) cell attachment. In both cases the FN is clearly seen in a compact shape before cell seeding and is rearranged into a more elongated shape after cell seeding and attachment. Cells have been removed in (B) and (D) (see text). (Scale bars: (A) 143 nm, (B) 158 nm, (C) 47 nm, (D) 57 nm).

FN adsorption analysis with AFM

To control the clustering of integrins it is important to know the number of adhesions per nanoisland. Nanopatterned surfaces were functionalized and the FN crosslinked with cell-impermeable amine-reactive BS[3] before and after cell seeding. AFM images of the surfaces before cell seeding show distinct ordered arrays of protein on the gold nanopatterns [Fig. 4(A,C)]. The protein clusters have an approximate size and height of 36 and 7 nm, respectively, which is in agreement with lateral dimensions of globular FN using electron microscopy.[70,71] The protein clusters also have a rounded or compact shape typical of FN adsorbed to hydrophobic surfaces,[66] and practically no protein was observed on the PEG-modified glass surface between the nanoislands, which is in agreement with our XPS and cell-seeding experiments. Taking each spherical entity as a single FN, there are ~60–70 FN proteins on each nanopattern for the 1500M surface [Fig. 4(A)] and 2 to 5 on the 0420M pattern [Fig. 4(C)], resulting in an approximate density of 714 $FN/\mu m^2$ on the pattern for each sample or an average of 55 $FN/\mu m^2$ for the composite surface, which includes the surrounding glass-PEG background. However, the XPS data indicate that a composite average of 217 $FN/\mu m^2$ should be measured for the monolayer surfaces, which is in agreement with the esti-mated total volume of 0.72 mL/g of FN.[72] This discrepancy may be induced by the BS[3] crosslinker used to secure the protein before AFM analysis by artificially enlarging the imaged proteins during the crosslinking process, or by making it difficult to distinguish between two separate proteins and thereby inducing a lower-than-actual protein count. Even though our measured FN dimensions appear in agreement with AFM measurements by others,[66] we have used the higher surface concentration of FN derived from the XPS-radiolabeling comparison for the following analysis. Still, the density of FN, averaged over the patterned and nonpatterned areas of a nanopatterned surface is very low. In comparison, endothelial cell adhesion has been shown on homogenous surfaces displaying as low as 250 $FN/\mu m^2$, but these surfaces led to reduced proliferation or cell death over time.[73]

We compared the FN morphology before cell seeding to its morphology after HUVECs adhered to and spread on the nanopatterned surfaces. After 1 day, all surface proteins were crosslinked and rinsed with SDS to remove the majority of each cell, leaving behind only cell sections that are crosslinked to the surface, or bare ECM in areas where no cells were attached at the time of crosslinking. In some areas, instead of displaying ordered arrays of clustered FN, the FN was rearranged or removed (Figures 4B and 4D). A reorganization of FN could be expected as
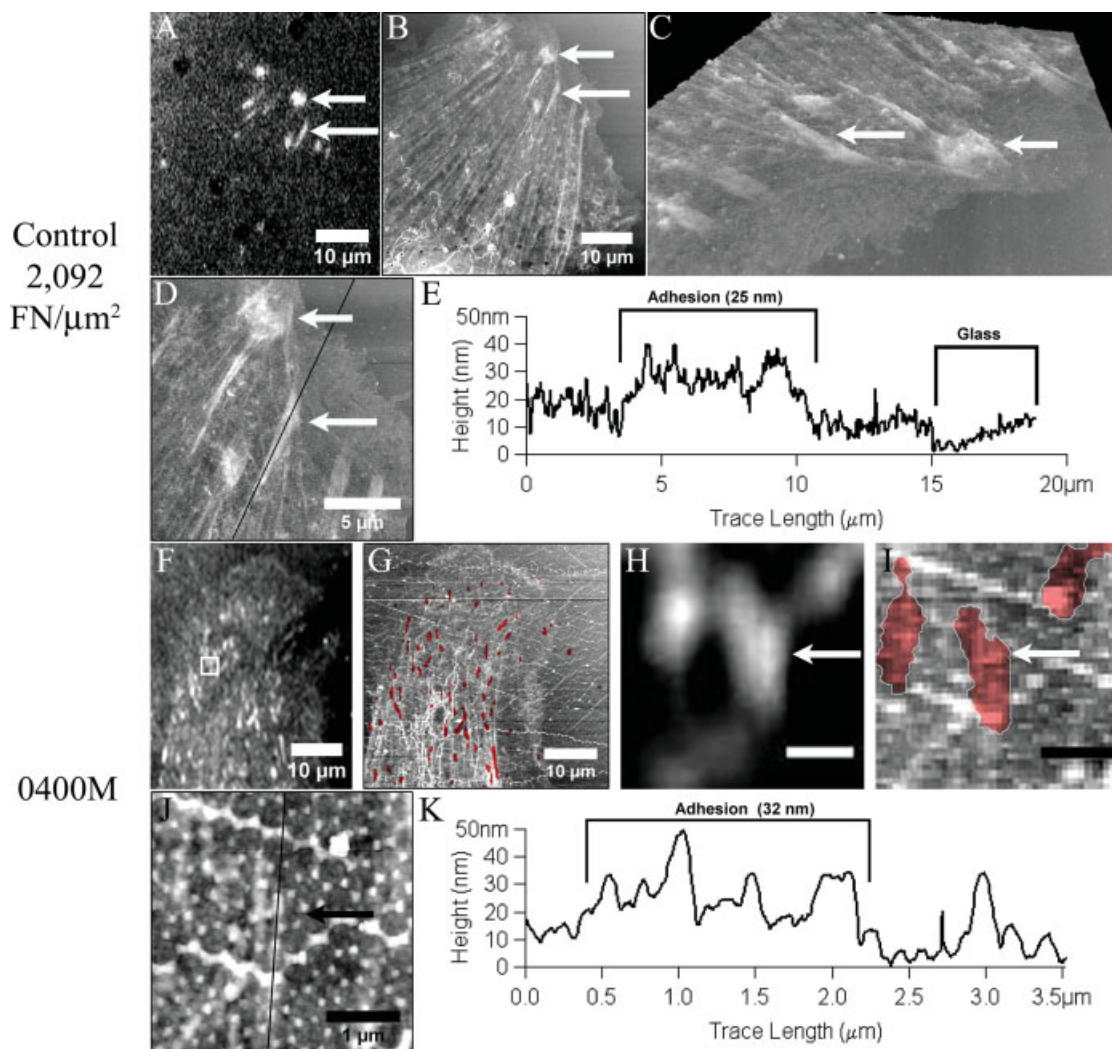
Figure 5. (A–E) Fixed HUVECs at 72 h on glass control. Corresponding images of (A) vinculin fluorescence of adhesions and (B) AFM topographic image of the same area, showing large adhesions located mainly at the cell periphery; (C) shows (B) in a 3D view. A dot and dash adhesion are indicated by a small and large arrow, respectively. (D) High-resolution AFM image of the two adhesions marked in (B). (E) Height trace corresponding to the line across the dash adhesion in (D) from bottom to top shown left to right. (F–K) Fixed HUVECs at 72 h on the 0400M pattern. (F) Vinculin fluorescence of adhesions and (G) AFM topographic image of the same area with the fluorescent adhesions from (F) overlaid in red (dark dots). The adhesions are much smaller and more evenly distributed than on the control surface. (H) and (I) show a zoomed-in view of the box area of (F) and (G), respectively, with the fluorescent areas in (H) overlaid in red and outlined in (I). (J) High-resolution AFM image of the same area as in (I) with the arrow marking an adhesion terminating on a nanopattern. (K) Height trace corresponding to the dotted line across the raised adhesion in (J) from bottom to top shown left to right. The adhesion structure is about 1.7-μm long, stretching from 0.5 to 2.2 μm along the trace. Adhesions in control and patterned samples are about 13–17 nm high after background correction (see text for details). Scale bar for H–J is 1 μm. [Color figure can be viewed in the online issue, which is available at www. interscience.wiley.com.]

the cells remodel and stretch FN as stress is applied during focal adhesion maturation and cell movement.[74]

Adhesion analysis

For proof of principle and to validate our claim that surfaces with nanoislands of FN surrounded by a passive background limit adhesion site size, we performed dual fluorescence and AFM imaging on

vinculin-containing adhesion sites. Figure 5 shows an example of cells fixed and immunostained for vinculin after 72 h on a nanopatterned (average density of 217 FN/μm^2) and a nonpatterned glass surface (2092 FN/μm^2). While the vinculin-containing adhesions on the glass control surface could be easily correlated between fluorescence and AFM images [Fig. 5(A-C)], on the nanopattern this matching was more difficult due to the small size of the adhesions. To positively confirm the location of vinculin-

containing adhesions in the AFM images, the fluorescence image was slightly scaled and overlaid on the AFM image using multiple points on the cell rim as alignment markers [Fig. 5(F)]. Fluorescently labeled adhesions closely matched increased height features in the AFM image across the entire cell [Fig. 5(G)]. The matched features were terminations of up to 20 μm long, thin nonfluorescent raised lines that could be traced across the cell, presumably actin microfilaments. High-resolution AFM scans [Fig. 5(J), white box in Fig. 5(F)] were then correlated using zoomed portions of Figure 5(F,G) as reference [Fig. 5(H,I)]. Although the adhesions incorporate a defect line in some instances, they most often do not align with the direction of defect lines and the overwhelming majority of the vinculin-stained areas are not on defects. The large, optically resolution-limited fluorescence areas decompose into single or double thin elongated features in the AFM images, as seen to the left and center in Figure 5(I,J), respectively. The optical resolution limitation does not allow us to determine whether the vinculin is localized exclusively over the nanopatterns, or whether it bridges between patterns.

Detailed AFM height measurements can give further insight into the structuring of the adhesions. The dash adhesion on the control glass surface [long arrow in Fig. 5(A–D)] had a measured height of ∼25 nm above the glass background, including an 8–10 nm contribution from the remainder of the cell membrane [Fig. 5(E)]. The adhesion on the 0400M [arrow in Fig. 5(H–J)] had a measured height of about 32 nm [Fig. 5(K)], including about 19 nm due to the height of the nanopattern, FN, and the cell membrane (measured independently). The adhesion site is therefore about 13–17 nm higher than the background in both the glass and the 0400M cases. Independent measurements on fiber structures on these samples give 7–9 nm height above background, which is close to the thickness of an actin microfilament of 7 nm in diameter.

Following the profile along the line in Figure 5(J) from top to bottom [right to left in Fig. 5(K)], starting with an adhesion-free area (∼7- to 8-nm thick) with a hole in the membrane and two nanopatterns, then rising to the adhesion on a nanopattern at 2.2 μm, continuing at about 20–22 nm height towards the next pattern at 1.5 μm, crossing a defect line at 1.0 μm, and one more nanopattern at 0.6 μm, before continuing at a reduced height of about 15 nm as actin fibers. These heights agree with the 13–17 nm for adhesions and the actin height of 7 nm above background. The height between each of the nanopatterns is close to the thickness of adhesions, which probably results from firmly crosslinked bridges between the raised adhesions on the patterns built from cytoplasmic components of adhesion complexes. The length of the

adhesion structure is about 1.7 μm, but it is only about 120-nm wide, which leads to a total area of 0.2 μm^2. The two adhesions in Figure 5(J) that together compose the vinculin fluorescence area are completely separated, as the height between them reaches background levels (not shown). The two lines join at around the defect line.

We also find a striking difference in the size and distribution of adhesions between control and nanopatterned surfaces. HUVECs on nonpatterned glass surfaces have large adhesions mostly at the cell periphery [Fig. 5(A,B)] ranging in size, for the cell analyzed here, from about 1–6 μm and in area from 6.8 to 7.3 μm^2 for a dot adhesion [short arrow Fig. 5(A,D)] and a dash adhesion [long arrow Fig. 5(A,D)], respectively, as determined from the AFM images. These adhesions act as terminating sites for multiple actin fibers as seen in the AFM images [Fig. 5(B,C)]. In contrast, HUVECs on the 0400M surface displayed a more homogenous distribution of small adhesions [Fig. 5(F)]. The adhesion site area for the adhesion indicated in Figure 5(H) is 0.036 μm^2 or 0.2 μm^2, depending on whether only the pattern or the full area indicated by vinculin staining is counted. In any case, this is far smaller than adhesions formed on the control surface. The smaller adhesions on the nanopatterned surfaces were coupled to fewer actin fibers [Fig. 5(I,J)], as opposed to multiple fibers seen in cells seeded on the glass surfaces. Although we provide here just a snapshot, more detailed investigations of combined AFM and fluorescence imaging are in progress, and we can conclude that HUVECs react to the nanopatterned surfaces by forming smaller and more distributed adhesions on the supporting pattern areas. Most importantly, the adhesions terminate in the pattern and can limit adhesion site growth. However, it appears likely that cytoplasmic components of adhesions can bridge between individual patterns, at least if the distance is not too great.

Influence of nanopatterned surfaces on cell proliferation

HUVECs were seeded on nanopatterned and control surfaces and their cell densities measured (Fig. 6). Proliferation rates were calculated by normalizing the measured density at each time point to the average cell seeding density at 4 h; these rates were used for statistical analysis. Figure 6(A) compares cell densities and proliferation rates for different pattern sizes. HUVECs were seeded on several nanopatterned surfaces with varying adhesion site sizes but with a constant average FN surface coverage of 7.2%. Initial attachment densities were similar for all patterns, as were the initial proliferation rates, which were in good agreement with literature values for
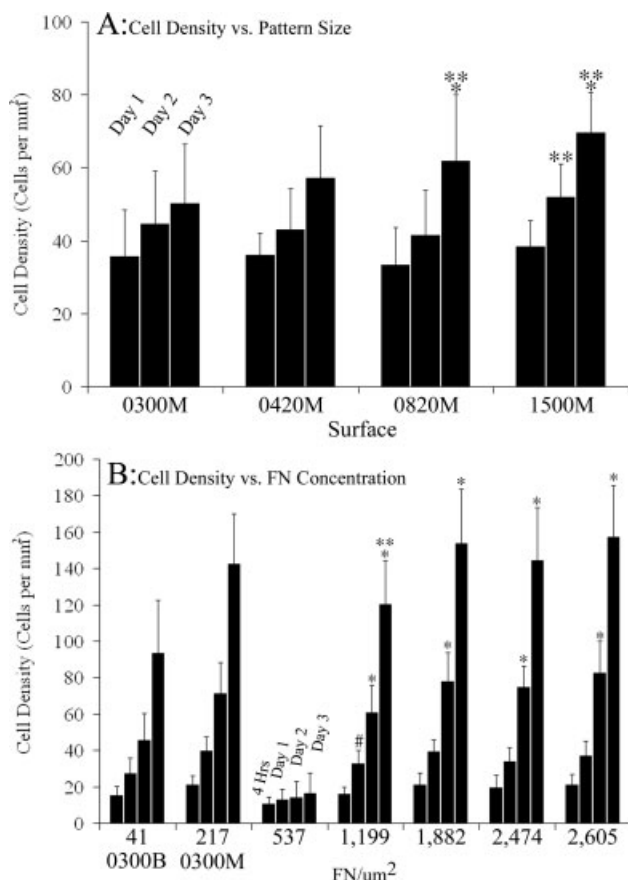
Figure 6. (A) Influence of the pattern size: Pooled HUVEC densities as a function of increasing nanopattern size for M-type samples, each at 24, 48, and 72 h. Statistical differences are given for proliferation, that is the cell density relative to the cell density at 4 h. Initial seeding densities are very similar for all patterns. A significant increase in cell proliferation ($p < 0.05$) was observed between the smaller and larger nanopatterned surfaces ($n = 20$, error bars = 1 SD). *Statistically higher proliferation rate compared with 0300M. **Statistically higher proliferation rate compared with 0420M. (B) Influence of the average FN density: Nonpooled HUVEC densities as a function of FN surface concentration ($FN/\mu m^2$) at 4, 24, 48, and 72 h of incubation. Surfaces displaying nanoclusters of FN can support adhesion and proliferation at orders of magnitude lower FN surface concentrations than homogenously coated surfaces. All surfaces induce significantly higher ($p < 0.002$) proliferation than the nonpatterned 537 $FN/\mu m^2$ surface at all times, including the initial seeding. While the 0300M surface shows statistically similar proliferation to the higher-density nonpatterned surfaces, the 0300B surface induces statistically significantly less proliferation at later time points than the higher-density nonpatterned surfaces ($n = 20$, error bars = 1 SD). *Statistically higher proliferation rate compared with 0300B ($p < 0.03$). **Statistically higher proliferation rate compared with 0300M ($p < 0.03$). #Statistically higher proliferation rate than the 2474 and 2605 $FN/\mu m^2$ surfaces ($p < 0.03$).

pooled HUVECs.[75] However, beginning after 48 h, but clearly after 72 h, HUVECs on the 0820M and 1500M surfaces displayed statistically significant increased proliferation compared with the 0300M

($p < 0.003$) and 0420M ($p < 0.04$) surfaces, indicating a trend of increased proliferation with increasing adhesion site size.

Figure 6(B) compares cell density and proliferation of HUVECs on the two smallest pattern sizes with 2.2 and 7.2% average FN surface coverage to cells seeded on nonpatterned FN-coated gold slides with FN densities ranging from 537 to 2605 $FN/\mu m^2$ at 4, 24, 48, and 72 h in culture. HUVECs were also seeded on a clean glass surface at a FN concentration of 10 $\mu g/mL$ (data not shown), and the cells responded similarly to cells on the gold surface at the same FN concentration. Initial cell-seeding densities after 4 h were significantly higher ($p \leq 0.001$) on both nanopatterned surfaces compared with the homogenously coated gold surface with the lowest FN surface density (537 $FN/\mu m^2$), even though the homogenously coated surface presents an order of magnitude higher average FN density compared with the 0300B nanopatterned surface. There was no significant difference in initial cell seeding densities between the nanopatterns and the nonpatterned higher ligand densities (>1199 $FN/\mu m^2$), implying that the ability to quickly cluster integrins to form well-defined adhesion sites is more influential in promoting initial cell attachment than the overall ligand surface density.

After 24 h, cells on 0300B proliferated at a statistically significant lower rate than on homogenously coated surfaces displaying at least 1199 $FN/\mu m^2$, and these differences were maintained for 3 days in culture ($p \leq 0.03$). The 0300M surface induced proliferation that was not statistically different from the homogenously coated surfaces of at least 1199 $FN/\mu m^2$ within a p-value of 0.3, but the proliferation difference compared with the highest nonpatterned density reached a p-value of 0.06 at 48 and 72 h. The 1199 $FN/\mu m^2$ sample is somewhat inconsistent, as it has higher proliferation than both the 0300M sample at 72 h and the highest density nonpatterned surface at 24 h [Fig. 6(B)]. This behavior could be caused by a partial breakdown of the BSA block and serum proteins adsorbing at later time points. The fact that the 0300M and 0300B samples are not significantly different, even though the 0300B sample is different from the higher density nonpatterned samples and the 0300M is not, suggests that there may be a gradual difference that may be resolved with a larger number of samples. We conclude that the adhesion site size and to some degree the pattern pitch are important regulators of proliferation, and this dependence is much more pronounced at later time points. However, the local ligand density is the most important determining parameter, as adhesion and proliferation are supported at average FN densities on the nanopatterns that are much lower than the lowest nonpatterned surface density that supports proliferation with 537 $FN/\mu m^2$.

Cell spreading area

The projected cell spreading area was measured at 24-h intervals for 3 days for glass control (2092 FN/ μm^2) and four nanopatterned surfaces. A lognormal distribution was used to cope with the high levels of skewness towards higher spreading areas.[76] ANOVA and a nonparametric statistical analysis were performed to take the skewed distribution into account. Results from both ANOVA (ln) and nonparametric (np) analysis techniques indicate that after 24 h the HUVECs on the nanopatterned surfaces spread significantly less ($p_{ln} \leq 0.07$, $p_{np} \leq 0.003$) than cells on nonpatterned control surfaces (Fig. 7). After 3 days in culture, the cell spreading area on the nanopatterned surfaces was no longer as significantly different ($p_{ln} \leq 0.45$, $p_{np} \leq 0.05$) from the glass control, yet the HUVEC spreading area on the largest nanopattern, 1500M, was significantly higher than cells on any of the other surfaces ($p_{ln} \leq 0.006$, $p_{np} < 0.0001$) (Fig. 7). The higher spreading on the 1500M nanopattern with an adhesion site area close to 0.1 μm^2 and a pitch of nearly 1 μm compared with the nonpatterned glass control could indicate the influence of the relatively large distance between individual adhesions or the beginning of a qualitatively different behavior that starts at around 0.1 μm^2 per adhesion, as suggested by the proliferation data (see: Influence of Nanopatterned Surfaces on Cell Proliferation).

DISCUSSION

Nanopattern fabrication and functionalization

Integrin binding to its ECM ligand and integrin clustering are synergistic events needed to induce signaling and the full engagement with the cytoskeleton. Cluster size is an indicator of the maturation of adhesions, which is driven by the applied force of the actomyosin machinery of the cell. The size of each cluster can range from about 30 nm for a trimer, to submicron-sized for motile cells, to many microns for fully matured adhesions. Because of this wide range of adhesion sizes, restrictions in the growth process induced by chemical patterns or nanotopographical surface features are expected to influence both the adhesion of adhesion-dependent cells and the events initiated and controlled by adhesion.

Nanotopographic surfaces created by a variety of techniques have been shown to influence cell adhesion in several ways, including promoting alignment to grooves,[77] decreasing seeding efficiency, adhesion strength, and spreading on nanopits,[78–80] as well as increasing cell adhesion, spreading area, and cytoskeletal formation on raised nanopatterns.[81,82] The mech-
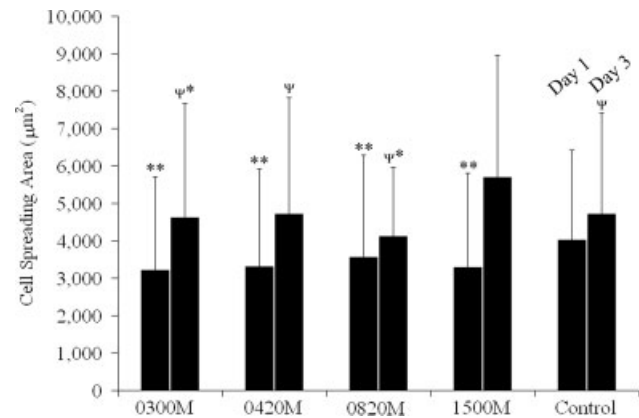

Figure 7. Measured average cell spreading areas on four nanopatterned surfaces and a glass control with 2092 FN/ μm^2. HUVECs on nanopatterned surfaces are significantly less spread than those on control surfaces after 1 day, but the significance decreases after 3 days. Cells on the 1500M surface spread much more than cells on nanopatterned and control surfaces after 3 days ($n = 107$, error bars = 1 SD (based on lognormal)). *Statistically significant ($p_{ln} \leq 0.45$, $p_{np} \leq 0.05$) less spreading than cells on control; **Statistically significant ($p_{ln} \leq 0.07$, $p_{np} \leq 0.003$) less spreading than cells on control; **Statistically significant ($p_{ln} \leq 0.006$, $p_{np} \leq 0.0001$) less spreading than cells on 1500M.

anism of nanotopography action is not clear, but increased filopodia formation,[83,84] Rac localization to the cell periphery,[81] and an upregulation of genes associated with cell signaling, proliferation, cytoskeletal components, and ECM production[82] have all been documented. While ECs and fibroblasts show increased cellular responses with decreasing nanotopography,[81] osteoblasts behave oppositely, displaying increased adhesion, proliferation, and deposition of extracellular calcium with increasing topography.[85–89] Nanotopographic surfaces have been suggested to induce selective adsorption of ECM proteins,[89] and while they demonstrate the importance of nanometer-scale features on cell behavior, they have so far not provided systematic insight into the connections between adhesion site properties and downstream cell behavior.

Chemically defined patterns of cell adhesion ligands, on the other hand, provide direct molecular control over the processes of cell adhesion as well as over the mechanics of force transduction. This control has been used very successfully to investigate cell adhesion, spreading, and differentiation on the micron scale with such tools as microcontact printing of thiols on gold. Cell adhesion size control down to 0.1 μm^2 using thiol stamping has shown that cells can adhere and spread well using such areas for integrin binding, unless the distance between the adhesion sites exceeds 2 μm.[50] The extension into nanometer-scale adhesion size control has been much more difficult, as serial lithography techniques, such

as dip-pen nanolithography,[44,90–93] other scanning probe lithography techniques,[94–97] and electron beam lithography,[98–100] are too time consuming in their fabrication to allow for systematic cell studies. Parallel patterning techniques such as imprint lithography,[101,102] micelle nanolithography,[103,104] particle lithography,[56] and capillary lithography[45] are better suited for quickly fabricating nanostructured surfaces over large areas.

Several nanopatterning techniques have been used to demonstrate cell adhesion,[105–107] but have so far not been used for systematic adhesion studies. These include capillary or imprint lithography,[45] molecular assembly patterning by lift-off (MAPL),[108,109] and variations of NSL.[110,111] Protein and cell adhesion have been observed on PEG pillars, but due to the repulsive properties of PEG, the level of cell adhesion was significantly lower than adhesion to similarly treated protein-coated glass surfaces.[45] Other techniques such as micelle lithography or star polymers have provided significant insights into the importance of integrin proximity in the clustering process, but they do not allow for the formation of larger adhesion sites except when used in conjunction with a serial technique such as e-beam lithography. Additionally, most techniques rely on RGD sequences for cell adhesion, and investigations of cell interactions with the full FN protein have not previously been possible on nanopatterns.

Experimental tools for systematic investigations to control the adhesion size from about 40 nm to about 300 nm, a size range in which a number of critical molecular and mechanical processes in cell adhesion may occur, have been missing so far. We have shown that NSL, a highly parallel self-assembly process, can be used to create large, cm^2-sized areas of nanopatterns of exactly this pattern size range, with defined size, spacing, and topography. These nanopatterned surfaces are a composite of two materials and can therefore be chemically modified with two distinct chemical functionalities. Our results with XPS, AFM, and cell-seeding experiments consistently show that modification of the glass background with PEG and thiolization of the gold nanostructures directs FN adsorption exclusively to the gold nanostructures. By performing the functionalization for both materials simultaneously, we minimized the PEG adsorption to the gold areas, and the lack of sulfur on the glass areas indicates no or little thiol on the PEG surface. The ability to immobilize the full FN on the gold areas enables the use of the synergistic sites in FN. The terminal functionality used here presents FN in a compact form similar to that found on nonpatterned hydrophobic surfaces,[66] but changing the thiol functionality to a hydrophilic end group would induce FN to appear in an extended form.[66] This flexibility would allow us to test the preferential engagement of different integrins based on the presentation of FN on different thiol terminal functionalities.[112,113] Although we have used noncovalent immobilization of FN on the nanopattern, the use of other functional thiols would allow specific and covalent anchoring by bioconjugation procedures. Of course, the presentation of small peptides tethered to thiols could also be easily achieved.

NSL has clear limitations: only two pattern size to spacing ratios can be achieved, resulting in a constant average FN surface density of 7.2% or 2.2% for M and B samples, respectively. Pattern size and spacing are coupled, but pattern pairs from M and B samples can be created that display similar adhesion site areas with varying interadhesion site spacing and vice versa. Since spheres are used as a mask, the choice of pattern shapes is strongly limited and mostly consists of triangles and disks, a limitation that, however, is unlikely to be important for the goal of adhesion size limitation. Also, as a self-assembly method, NSL has defects that possibly could present additional adhesion sites. However, we have not found an effect on cell behavior attributed to the inherent defects in the patterns fabricated by NSL, and Figure 5(I,J) show that the extensions terminate on small patterns, even though the possibility for attachment to defects is present. Although we have not found the limitations of NSL to have a significant influence on cell behavior in our experiments, a second generation of large-scale nanopatterned surfaces using nanoscale orthogonal biofunctionalization imprint lithography to create defect-free surfaces with a wide range of pattern properties is being developed.[102]

Nanopattern influence on endothelial cell behavior

Studies using homogenous surfaces have shown a direct correlation between FN surface density and endothelial and epithelial cell proliferation and spreading.[73,114] The selective adhesion of FN to nanopatterned surfaces changes the overall average density of FN, and allows comparative studies of cell attachment, spreading, and proliferation between overall and local densities of FN. As confirmed by XPS, M-type and B-type nanopatterned surfaces contain 7–8% and 2%, respectively, of the saturation amount of FN on a homogenous gold surface, in agreement with the average surface coverage of the pattern. We could show that seeding density as well as proliferation are mostly not determined by the average FN density, as cells on both the 7% and the 2% coverage surfaces seeded and proliferated far better than on the ~20% (537 FN/μm^2) coverage nonpatterned surface, and at average FN concentrations more than 10 times lower than would support

cell proliferation on homogeneously coated FN surfaces found in earlier studies.[73]

At later time points, pattern size and possibly pitch become important, as indicated by the significantly lower proliferation of cells on 0300M and 0420M samples relative to cells on the larger pattern sizes, and by the lower proliferation of cells on the 0300B sample compared with cells on the high-density nonpatterned samples. The time dependence of our proliferation results suggests that initially the local FN density is important to support fast cluster formation of integrins regardless of adhesion site size. Since homogenous substrates with low levels of FN are randomly covered and the nanopatterns induce the formation of discrete adhesion sites of densely packed FN, nonpatterned surfaces would need a far denser coating to support the same local density of adhesions, as has been suggested recently with experiments on larger cluster sizes.[43,46,50] At later time points proliferation is influenced not only by the local FN density, but also by adhesion size and possibly by the distance between adhesions. On the high-density nonpatterned surfaces adhesions are not limited in size, while on the small nanopatterns the restriction of an adhesion to below a threshold pattern size between 250 nm (0800M) and 100 nm (0420M) leads to slower proliferation. This corresponds to somewhere between 20 and 90 densely packed FNs per nanoisland. Also, it is interesting to note that the lowest nonpatterned FN surface concentration, which has an average density of 537 FN/μm^2 and very low cell proliferation rates, has an average distance between FN molecules of 43 nm. This value is below the 58–70 nm separation between cyclic RGDs found to be the threshold to support fibroblast adhesion using nanopatterned cyclic RGD.[43] This discrepancy could be explained either by the fact that in that study adhesion and spreading but not proliferation were tested, or otherwise by an inhomogeneous distribution of FN in our nonpatterned experiments or by a significant portion of the adsorbed FN having inaccessible binding sites.

Similar to proliferation, cell spreading area is commonly used to determine cellular reaction to a substrate. Endothelial cell spreading and proliferation have been linked: as the FN concentration on a surface increases, so do both the extent of cell spreading and the proliferation rates.[73] Nanotopographic surfaces have shown the ability to increase cell spreading in both endothelial cells[86] and fibroblasts,[82] while very high nanocolumns (160 nm) can reverse this effect in fibroblasts.[84] We show reduced spreading with HUVECs seeded onto FN nanopatterns with minimal topography of 10–13 nm compared with the nonpatterned controls after 24 h. Our HUVEC results show the opposite tendency to endothelial cells isolated from human tendon granuloma on 13-nm high

random topography.[86] This discrepancy could be a result of different cell types or due to differences in the surface properties and ECM adsorption. The fact that HUVECs on the 1500M surfaces with an individual adhesion site area of $\sim$0.1 μm^2 and an interadhesion site spacing of 0.9 μm spread more after 72 h than on a glass control could be attributed to the large spacing between the adhesion site areas. However, the cells on 1500M surfaces also spread more than on surfaces with smaller nanopatterns, which correlates with the increase in proliferation starting around 0.04 μm^2, suggesting that there is a different quality to the adhesion for adhesion sizes above $\sim$0.04 μm^2. Experiments to systematically probe the cell adhesive behavior for adhesion site areas of 0.01–0.05 μm^2 are in progress.

A threshold of 0.01–0.05 μm^2 for a single adhesion area is interesting, as this area is less than half the smallest pattern of 0.1 μm^2 investigated by Lehnert et al.[50] Their results showed that such a pattern leads to cell behavior indistinguishable from homogeneously coated surfaces as long as the distance between adhesions (pitch) was below 2 μm. Such a threshold is far smaller than the 1 μm^2 threshold found in force studies. Cellular traction and force studies have shown a linear relationship between adhesion site size and the force applied to the surface for adhesion sites larger than 1 μm^2, with larger adhesions applying higher forces per adhesion area.[27,115,116] Similar studies have also shown an inverse trend, with adhesions smaller than 1 μm^2 at the leading edge of cell movement applying higher forces per attachment area than larger adhesions.[27,117] Additionally, it has been shown that larger well-spread cells exert more force on the surface than smaller rounded cells.[118]

Vinculin and AFM imaging suggest a difference between the size and distribution of adhesions, with large adhesions mainly along the cell perimeter on a glass control, and small adhesions distributed more evenly across the cell for the nanopatterned surfaces. These data taken from a few cells need to be studied systematically and a study of the adhesion size and distribution induced by the nanopattern is in preparation. Our analysis of individual adhesions, as characterized by vinculin stains and AFM height scans, has shown that cellular adhesions are located at nanopatterns, although the adhesion complex may bridge between patterns. The complexes can therefore reach lengths in the micron range, but their width is only around 120 nm, leading to adhesion areas well below 1 μm^2. This corresponds to the nanoisland size used here, and preliminary data suggest that this correlation between width of the adhesion and nanoisland size holds for other patterns; further studies into this relationship are under way. The adhesion sites are linked to long elongated structures which are most

likely actin microfilaments. Although we have been unable to perform dual-label experiments for adhesions and actin with the current fluorescence microscope AFM combination, we have consistently seen with double-label experiments that adhesions on all nanopatterns are endpoints of actin fibers. Additionally, the height measured with AFM matches the thickness of microfilaments of 7 nm. The 13–17 nm height of the adhesions is independent of their lateral dimensions on nanopattern and control surfaces alike. Our AFM results of the HUVEC adhesions on glass agree qualitatively with earlier studies, except that our adhesion height is lower than found for large adhesions of rat embryo fibroblasts after 72 h on glass surfaces that had been de-roofed to allow for AFM analysis of the adhesions in cytosolic buffer.[119] We attribute this to our much more rigid crosslinking and imaging in air that could lead to a more collapsed structure.

While the nanopattern clearly influences the size and distribution of adhesions, it appears that the adhesions can sometimes bridge several patterns. The question therefore arises whether integrins are limited to the nanopatterns and the cytoplasmic components, such as vinculin, are able to bridge, or whether the integrins are also anchoring to the surfaces between the patterns. Although we do not have a positive proof at this time, XPS analysis has shown almost no FN between the nanoislands, cell reseeding after 3 days in medium containing culture has shown little increase in the cells' ability to adhere to PEGylated surfaces, and AFM scans have shown little evidence for FN outside the pattern before and after cell seeding. However, further experiments on the distribution of integrins and other cytoplasmic adhesion proteins are ongoing to determine which adhesion components can bridge the gap between two individual nanoislands, and what maximum distance can be bridged. Furthermore, the coupling of fewer actin fibers to the adhesions on nanopatterned surfaces than on nonpatterned surfaces supports our view that mechanotransduction and the application of force to the surface is key to the modulation of cell behavior by adhesion size restriction.

It is interesting to further compare cellular mechanotransduction on homogeneous but elastic substrates with our rigid but nanopatterned substrates. ECs on elastic substrates show a strong correlation between elastic modulus and spreading, while proliferation is unaffected.[24] Our findings of a relatively small proliferation decrease and decreased cell spreading of ECs on smaller nanopatterns suggests that restricting integrin clustering with nanopatterns and reducing force generation at adhesion sites with elastic surfaces may induce changes in cell behavior through a similar pathway. Considering the importance of cellular mechanotransduction for cell differ-

entiation and phenotype,[120] the nanopatterned surfaces presented here to control integrin clustering could provide a complementary tool to elastic substrates for understanding the molecular mechanisms of integrin-mediated mechanotransduction. Further studies relating focal adhesion properties to cytoskeletal formation and cell motility will elucidate these questions.

CONCLUSIONS

We have demonstrated a fabrication technique to create nanopatterned surfaces with dual chemical functionality that allow for directed protein adsorption on nanoislands from 90 to 400 nm in size. Cells adhere to the fibronectin residing on these nanoislands and fibronectin is rearranged after cell adhesion. The cells build anchor sites that are directed to the nanoislands, but the cytoplasmic complex of the adhesions may be able to bridge between close adhesions. Adhesions are much smaller and more homogenously distributed on the nanopattern than on control surfaces. Proliferation at all times and on all nanopattern sizes tested is far higher than on nonpatterned surfaces of equivalent or up to 10 times higher average FN surface concentration. The nanopatterned surfaces induce changes in proliferation that depend on time. Early proliferation is independent of pattern size and equivalent to that seen on high surface density nonpatterned surfaces. Later, the proliferation is influenced by pattern pitch, or average FN surface density, and pattern size below ~ 0.05 μm^2. The FN nanoclustering also induces changes in the HUVEC spreading area, with initially less spreading on all patterned surfaces than on control. After 72 h the difference becomes less significant, but again the ~ 0.1 μm^2-sized pattern induces a higher spreading then all other samples. The observed changes in cell behavior on the nanopatterned surfaces are not merely a result of the average density of ECM proteins, but indicate a balance of local FN density, adhesion size, and distance between adhesions. The results for cells seeded on chemically nanopatterned surfaces suggest an important role of the forces the cell can exert onto the surface via its adhesions, and paint a complementary picture on rigid nanopatterned surfaces to cells seeded on elastic substrates. Because of the differences seen for cells adhering to nanoislands below a size of 0.1 μm^2, the results highlight the importance of this size range of very small adhesions for cell signaling. Our approach may therefore provide a new view on the molecular mechanisms of cellular mechanotransduction and the development of tissue engineering constructs.

References

1. Hynes RO. Integrins—Versatility, Modulation, and Signaling in Cell-Adhesion. Cell 1992;69:11–25.
2. Short SM, Talbott GA, Juliano RL. Integrin-mediated signaling events in human endothelial cells. Mol Biol Cell 1998;9:1969–1980.
3. Miranti CK, Brugge JS. Sensing the environment: A historical perspective on integrin signal transduction. Nature Cell Biol 2002;4:E83–E90.
4. Ruegg C, Mariotti A. Vascular integrins: Pleiotropic adhesion and signaling molecules in vascular homeostasis and angiogenesis. Cell Mol Life Sci 2003;60:1135–1157.
5. Liddington RC, Ginsberg MH. Integrin activation takes shape. J Cell Biol 2002;158:833–839.
6. Miyamoto S, Akiyama SK, Yamada KM. Synergistic roles for receptor occupancy and aggregation in integrin transmembrane function. Science 1995;267:883–885.
7. Miyamoto S, Teramoto H, Coso OA, Gutkind JS, Burbelo PD, Akiyama SK, Yamada KM. Integrin Function—Molecular hierarchies of cytoskeletal and signaling molecules. J Cell Biol 1995;131:791–805.
8. Coussen F, Choquet D, Sheetz MP, Erickson HP. Trimers of the fibronectin cell adhesion domain localize to actin filament bundles and undergo rearward translocation. J Cell Sci 2002;115:2581–2590.
9. Briesewitz R, Kern A, Marcantonio EE. Ligand-dependent and ligand-independent integrin focal contact localization—The role of the alpha-chain cytoplasmic domain. Mol Biol Cell 1993;4:593–604.
10. Geiger B, Bershadsky A, Pankov R, Yamada KM. Transmembrane extracellular matrix-cytoskeleton crosstalk. Nat Rev Mol Cell Biol 2001;2:793–805.
11. Cohen M, Joester D, Geiger B, Addadi L. Spatial and temporal sequence of events in cell adhesion: From molecular recognition to focal adhesion assembly. Chembiochem 2004;5:1393–1399.
12. Geiger B, Bershadsky A. Assembly and mechanosensory function of focal contacts. Curr Opin Cell Biol 2001;13:584–592.
13. Zaidel-Bar R, Cohen M, Addadi L, Geiger B. Hierarchical assembly of cell-matrix adhesion complexes. Biochem Soc Trans 2004;32:416–420.
14. Mostafavi-Pour Z, Askari JA, Parkinson SJ, Parker PJ, Ng TTC, Humphries MJ. Integrin-specific signaling pathways controlling focal adhesion formation and cell migration. J Cell Biol 2003;161:155–167.
15. Lauffenburger DA, Wells A. Getting a grip: New insights for cell adhesion and traction. Nat Cell Biol 2001;3:E110–E112.
16. Sieg DJ, Hauck CR, Schlaepfer DD. Required role of focal adhesion kinase (FAK) for integrin-stimulated cell migration. J Cell Sci 1999;112:2677–2691.
17. Li S, Huang NF, Hsu S. Mechanotransduction in endothelial cell migration. J Cell Biochem 2005;96:1110–1126.
18. Sastry SK, Lakonishok M, Wu S, Truong TQ, Huttenlocher A, Turner CE, Horwitz AF. Quantitative changes in integrin and focal adhesion signaling regulate myoblast cell cycle withdrawal. J Cell Biol 1999;144:1295–1309.
19. Meredith DO, Owen GR, ap Gwynn I, Richards RG. Variation in cell-substratum adhesion in relation to cell cycle phases. Exp Cell Res 2004;293:58–67.
20. Wary KK, Mainiero F, Isakoff SJ, Marcantonio EE, Giancotti FG. The adaptor protein Shc couples a class of integrins to the control of cell cycle progression. Cell 1996;87:733–743.
21. Almeida EAC, Ilic D, Han Q, Hauck CR, Jin F, Kawakatsu H, Schlaepfer DD, Damsky CH. Matrix survival signaling: From fibronectin via focal adhesion kinase to c-Jun NH2-terminal kinase. J Cell Biol 2000;149:741–754.
22. Scatena M, Almeida M, Chaisson ML, Fausto N, Nicosia RF, Giachelli CM. NF-kappa B mediates alpha v beta 3 integrin-induced endothelial cell survival. J Cell Biol 1998;141:1083–1093.
23. Discher DE, Janmey P, Wang YL. Tissue cells feel and respond to the stiffness of their substrate. Science 2005;310:1139–1143.
24. Yeung T, Georges PC, Flanagan LA, Marg B, Ortiz M, Funaki M, Zahir N, Ming WY, Weaver V, Janmey PA. Effects of substrate stiffness on cell morphology, cytoskeletal structure, and adhesion. Cell Motil Cytoskeleton 2005;60:24–34.
25. Paszek MJ, Zahir N, Johnson KR, Lakins JN, Rozenberg GI, Gefen A, Reinhart-King CA, Margulies SS, Dembo M, Boettiger D, Hammer DA, Weaver VM. Tensional homeostasis and the malignant phenotype. Cancer Cell 2005;8:241–254.
26. Bershadsky AD, Balaban NQ, Geiger B. Adhesion-dependent cell mechanosensitivity. Annu Rev Cell Dev Biol 2003;19:677–695.
27. Tan JL, Tien J, Pirone DM, Gray DS, Bhadriraju K, Chen CS. Cells lying on a bed of microneedles: An approach to isolate mechanical force. Proc Natl Acad Sci USA 2003;100:1484–1489.
28. du Roure O, Saez A, Buguin A, Austin RH, Chavrier P, Siberzan P, Ladoux B. Force mapping in epithelial cell migration. Proc Natl Acad Sci USA 2005;102:2390–2395.
29. Dimilla PA, Stone JA, Quinn JA, Albelda SM, Lauffenburger DA. Maximal migration of human smooth-muscle cells on fibronectin and type-IV collagen occurs at an intermediate attachment strength. J Cell Biol 1993;122:729–737.
30. Gupton SL, Waterman-Storer CM. Spatiotemporal feedback between actomyosin and focal-adhesion systems optimizes rapid cell migration. Cell 2006;125:1361–1374.
31. Vogel V, Sheetz M. Local force and geometry sensing regulate cell functions. Nat Rev Mol Cell Biol 2006;7:265–275.
32. Jiang GY, Giannone G, Critchley DR, Fukumoto E, Sheetz MP. Two-piconewton slip bond between fibronectin and the cytoskeleton depends on talin. Nature 2003;424:334–337.
33. Choquet D, Felsenfeld DP, Sheetz MP. Extracellular matrix rigidity causes strengthening of integrin-cytoskeleton linkages. Cell 1997;88:39–48.
34. Schmidt CE, Horwitz AF, Lauffenburger DA, Sheetz MP. Integrin cytoskeletal interactions in migrating fibroblasts are dynamic, asymmetric, and regulated. J Cell Biol 1993;123:977–991.
35. Felsenfeld DP, Choquet D, Sheetz MP. Ligand binding regulates the directed movement of beta 1 integrins on fibroblasts. Nature 1996;383:438–440.
36. Mrksich M, Whitesides GM. Patterning self-assembled monolayers using microcontact printing—A new technology for biosensors. Trends Biotechnol 1995;13:228–235.
37. Xia YN, Whitesides GM. Soft lithography. Annu Rev Mater Sci 1998;28:153–184.
38. Winkelmann M, Gold J, Hauert R, Kasemo B, Spencer ND, Brunette DM, Textor M. Chemically patterned, metal oxide based surfaces produced by photolithographic techniques for studying protein- and cell-surface interactions I: Microfabrication and surface characterization. Biomaterials 2003;24:1133–1145.
39. McFarland CD, Thomas CH, DeFilippis C, Steele JG, Healy KE. Protein adsorption and cell attachment to patterned surfaces. J Biomed Mater Res 2000;49:200–210.

40. Sorribas H, Padeste C, Tiefenauer L. Photolithographic generation of protein micropatterns for neuron culture applications. Biomaterials 2002;23:893–900.

41. Chen CS, Mrksich M, Huang S, Whitesides GM, Ingber DE. Geometric control of cell life and death. Science 1997;276:1425–1428.

42. Chen CS, Jiang XY, Whitesides GM. Microengineering the environment of mammalian cells in culture. MRS Bullet 2005;30:194–201.

43. Arnold M, Cavalcanti-Adam EA, Glass R, Blummel J, Eck W, Kantlehner M, Kessler H, Spatz JP. Activation of integrin function by nanopatterned adhesive interfaces. Chemphyschem 2004;5:383–388.

44. Lee KB, Park SJ, Mirkin CA, Smith JC, Mrksich M. Protein nanoarrays generated by dip-pen nanolithography. Science 2002;295:1702–1705.

45. Kim P, Kim DH, Kim B, Choi SK, Lee SH, Khademhosseini A, Langer R, Suh KY. Fabrication of nanostructures of polyethylene glycol for applications to protein adsorption and cell adhesion. Nanotechnology 2005;16:2420–2426.

46. Koo LY, Irvine DJ, Mayes AM, Lauffenburger DA, Griffith LG. Co-regulation of cell adhesion by nanoscale RGD organization and mechanical stimulus. J Cell Sci 2002;115:1423–1433.

47. Maheshwari G, Brown G, Lauffenburger DA, Wells A, Griffith LG. Cell adhesion and motility depend on nanoscale RGD clustering. J Cell Sci 2000;113:1677–1686.

48. Comisar WA, Hsiong SX, Kong HJ, Mooney DJ, Linderman JJ. Multi-scale modeling to predict ligand presentation within RGD nanopatterned hydrogels. Biomaterials 2006;27:2322–2329.

49. Walter N, Selhuber C, Kessler H, Spatz JP. Cellular unbinding forces of initial adhesion processes on nanopatterned surfaces probed with magnetic tweezers. Nano Lett 2006;6:398–402.

50. Lehnert D, Wehrle-Haller B, David C, Weiland U, Ballestrem C, Imhof BA, Bastmeyer M. Cell behaviour on micropatterned substrata: Limits of extracellular matrix geometry for spreading and adhesion. J Cell Sci 2004;117:41–52.

51. Garcia AJ, Takagi J, Boettiger D. Two-stage activation for alpha(5)beta(1) integrin binding to surface-adsorbed fibronectin. J Biol Chem 1998;273:34710–34715.

52. Zaidel-Bar R, Ballestrem C, Kam Z, Geiger B. Early molecular events in the assembly of matrix adhesions at the leading edge of migrating cells. J Cell Sci 2003;116:4605–4613.

53. Zimerman B, Volberg T, Geiger B. Early molecular events in the assembly of the focal adhesion-stress fiber complex during fibroblast spreading. Cell Motil Cytoskeleton 2004;58:143–159.

54. Deckman HW, Dunsmuir JH. Natural lithography. Appl Phys Lett 1982;41:377–379.

55. Haynes CL, Van Duyne RP. Nanosphere lithography: A versatile nanofabrication tool for studies of size-dependent nanoparticle optics. J Phys Chem B 2001;105:5599–5611.

56. Garno JC, Amro NA, Wadu-Mesthrige K, Liu GY. Production of periodic arrays of protein nanostructures using particle lithography. Langmuir 2002;18:8186–8192.

57. Hulteen JC, Vanduyne RP. Nanosphere lithography—A materials general fabrication process for periodic particle array surfaces. J Vacuum Sci Technol 1995;13:1553–1558.

58. Matsushita SI, Yagi Y, Miwa T, Tryk DA, Koda T, Fujishima A. Light propagation in composite two-dimensional arrays of polystyrene spherical particles. Langmuir 2000;16:636–642.

59. Matsushita SI, Miwa T, Fujishima A. Stable two-dimensional fine-particle arrays in solution. Langmuir 2001;17:988–992.

60. Papra A, Gadegaard N, Larsen NB. Characterization of ultrathin poly(ethylene glycol) monolayers on silicon substrates. Langmuir 2001;17:1457–1460.

61. Lee MH, Ducheyne P, Lynch L, Boettiger D, Composto RJ. Effect of biomaterial surface properties on fibronectin-alpha(5)beta(1) integrin interaction and cellular attachment. Biomaterials 2006;27:1907–1916.

62. Sharma S, Johnson RW, Desai TA. XPS and AFM analysis of antifouling PEG interfaces for microfabricated silicon biosensors. Biosens Bioelectron 2004;20:227–239.

63. Lhoest JB, Detrait E, van den Bosch de Aguilar P, Bertrand P. Fibronectin adsorption, conformation, and orientation on polystyrene substrates studied by radiolabeling, XPS, and ToF SIMS. J Biomed Mater Res 1998;41:95–103.

64. Zhu YB, Chian KS, Chan-Park MB, Mhaisalkar PS, Ratner BD. Protein bonding on biodegradable poly(L-lactide-co-caprolactone) membrane for esophageal tissue engineering. Biomaterials 2006;27:68–78.

65. Garcia AJ, Vega MD, Boettiger D. Modulation of cell proliferation and differentiation through substrate-dependent changes in fibronectin conformation. Mol Biol Cell 1999;10:785–798.

66. Bergkvist M, Carlsson J, Oscarsson S. Surface-dependent conformations of human plasma fibronectin adsorbed to silica, mica, and hydrophobic surfaces, studied with use of Atomic Force Microscopy. J Biomed Mater Res A 2003;64:349–356.

67. Ratner BD, Castner DG. Electron Spectroscopy for Chemical Analysis. In: Vickerman JC, Editor. Surface Analysis: The Principal Techniques. West Sussex: John Wiley & Sons, Inc.; 1997. p 43–98.

68. Tidwell CD, Castner DG, Golledge SL, Ratner BD, Meyer K, Hagenhoff B, Benninghoven A. Static time-of-flight secondary ion mass spectrometry and X-ray photoelectron spectroscopy characterization of adsorbed albumin and fibronectin films. Surf Interface Anal 2001;31:724–733.

69. Galtayries A, Warocquier-Clerout R, Nage MD, Marcus P. Fibronectin adsorption on Fe-Cr alloy studied by XPS. Surf Interface Anal 2006;38:186–190.

70. Price TM, Rudee ML, Pierschbacher M, Ruoslahti E. Structure of fibronectin and its fragments in electron-microscopy. Eur J Biochem 1982;129:359–363.

71. Erickson HP, Carrell NA. Fibronectin in extended and compact conformations—electron-microscopy and sedimentation analysis. J Biol Chem 1983;258:4539–4544.

72. Rocco M, Carson M, Hantgan R, McDonagh J, Hermans J. Dependence of the shape of the plasma fibronectin molecule on solvent composition - ionic-strength and glycerol content. J Biol Chem 1983;258:4545–4549.

73. Ingber DE. Fibronectin controls capillary endothelial-cell growth by modulating cell-shape. Proc Natl Acad Sci USA 1990;87:3579–3583.

74. Vogel V, Baneyx G. The tissue engineering puzzle: A molecular perspective. Annu Rev Biomed Eng 2003;5:441–463.

75. Miura M, Fujimoto K. Subcellular topological effect of particle monolayers on cell shapes and functions. Colloids Surf B 2006;53:245–253.

76. Truskey GA, Pirone JS. The effect of fluid shear-stress upon cell-adhesion to fibronectin-treated surfaces. J Biomed Mater Res 1990;24:1333–1353.

77. Teixeira AI, Abrams GA, Bertics PJ, Murphy CJ, Nealey PF. Epithelial contact guidance on well-defined micro- and nanostructured substrates. J Cell Sci 2003;116:1881–1892.

78. Curtis ASG, Gadegaard N, Dalby MJ, Riehle MO, Wilkinson CDW, Aitchison G. Cells react to nanoscale order and symmetry in their surroundings. IEEE Trans Nanobiosci 2004;3: 61–65.

79. Martines E, McGhee K, Wilkinson C, Curtis A. A parallel-plate flow chamber to study initial cell adhesion on a nano-featured surface. IEEE Trans Nanobiosci 2004;3:90–95.

80. Dalby MJ, Gadegaard N, Riehle MO, Wilkinson CDW, Curtis ASG. Investigating filopodia sensing using arrays of defined nano-pits down to 35 nm diameter in size. Int J Biochem Cell Biol 2004;36:2005–2015.

81. Dalby MJ, Giannaras D, Riehle MO, Gadegaard N, Affrossman S, Curtis ASG. Rapid fibroblast adhesion to 27 nm high

polymer demixed nano-topography. Biomaterials 2004;25: 77–83.

82. Dalby MJ, Yarwood SJ, Riehle MO, Johnstone HJH, Affrossman S, Curtsi ASG. Increasing fibroblast response to materials using nanotopography: Morphological and genetic measurements of cell response to 13-nm-high polymer demixed islands. Exp Cell Res 2002;276:1–9.

83. Dalby MJ, Riehle MO, Johnstone H, Affrossman S, Curtis ASG. Investigating the limits of filopodial sensing: A brief report using SEM to image the interaction between 10 nm high nano-topography and fibroblast filopodia. Cell Biol Int 2004;28:229–236.

84. Dalby MJ, Riehle MO, Sutherland DS, Agheli H, Curtis ASG. Changes in fibroblast morphology in response to nano-columns produced by colloidal lithography. Biomaterials 2004;25:5415–5422.

85. Zinger O, Anselme K, Denzer A, Habersetzer P, Wieland M, Jeanfils J, Hardouin P, Landolt D. Time-dependent morphology and adhesion of osteoblastic cells on titanium model surfaces featuring scale-resolved topography. Biomaterials 2004;25:2695–2711.

86. Dalby MJ, Riehle MO, Johnstone H, Affrossman S, Curtis ASG. In vitro reaction of endothelial cells to polymer demixed nanotopography. Biomaterials 2002;23:2945–2954.

87. Palin E, Liu HN, Webster TJ. Mimicking the nanofeatures of bone increases bone-forming cell adhesion and proliferation. Nanotechnology 2005;16:1828–1835.

88. Webster TJ, Siegel RW, Bizios R. Nanoceramic surface roughness enhances osteoblast and osteoclast functions for improved orthopaedic/dental implant efficacy. Scr Mater 2001;44:1639–1642.

89. Webster TJ, Ergun C, Doremus RH, Siegel RW, Bizios R. Specific proteins mediate enhanced osteoblast adhesion on nanophase ceramics. J Biomed Mater Res 2000;51:475–483.

90. Piner RD, Zhu J, Xu F, Hong SH, Mirkin CA. "Dip-pen" nanolithography. Science 1999;283:661–663.

91. Wilson DL, Martin R, Hong S, Cronin-Golomb M, Mirkin CA, Kaplan DL. Surface organization and nanopatterning of collagen by dip-pen nanolithography. Proc Natl Acad Sci USA 2001;98:13660–13664.

92. Ginger DS, Zhang H, Mirkin CA. The evolution of dip-pen nanolithography. Angew Chem Int Ed 2004;43:30–45.

93. Lee SW, Oh BK, Sanedrin RG, Salaita K, Fujigaya T, Mirkin CA. Biologically active protein nanoarrays generated using parallel dip-pen nanolithography. Adv Mater 2006;18:1133-1136.

94. Liu GY, Xu S, Qian YL. Nanofabrication of self-assembled monolayers using scanning probe lithography. Acc Chem Res 2000;33:457–466.

95. Wadu-Mesthrige K, Amro NA, Garno JC, Xu S, Liu GY. Fabrication of nanometer-sized protein patterns using atomic force microscopy and selective immobilization. Biophys J 2001;80:1891–1899.

96. Xu S, Miller S, Laibinis PE, Liu GY. Fabrication of nanometer scale patterns within self-assembled monolayers by nanografting. Langmuir 1999;15:7244–7251.

97. Wadu-Mesthrige K, Xu S, Amro NA, Liu GY. Fabrication and imaging of nanometer-sized protein patterns. Langmuir 1999;15:8580–8583.

98. Rundqvist J, Hoh JH, Haviland DB. Directed immobilization of protein-coated nanospheres to nanometer-scale patterns fabricated by electron beam lithography of poly(ethylene glycol) self-assembled monolayers. Langmuir 2006;22:5100–5107.

99. Zhang GJ, Tanii T, Zako T, Hosaka T, Miyake T, Kanari Y, Funatsu TW, Ohdomari I. Nanoscale patterning of protein using electron beam lithography of organosilane self-assembled monolayers. Small 2005;1:833–837.

100. Kunzi PA, Lussi J, Aeschimann L, Danuser G, Textor M, de Rooij NF, Staufer U. Nanofabrication of protein-patterned substrates for future cell adhesion experiments. Microelectron Eng 2005;78/79:582–586.

101. Hoff JD, Cheng LJ, Meyhofer E, Guo LJ, Hunt AJ. Nanoscale protein patterning by imprint lithography. Nano Lett 2004;4:853–857.

102. Gaubert HE, Frey W. Highly parallel fabrication of nanopatterned surfaces with nanoscale orthogonal biofunctionalization imprint lithography. Nanotechnology 2007;18:135101:1–7.

103. Haupt M, Ladenburger A, Sauer R, Thonke K, Glass R, Roos W, Spatz JP, Rauscher H, Riethmuller S, Moller M. Ultraviolet-emitting ZnO nanowhiskers prepared by a vapor transport process on prestructured surfaces with self-assembled polymers. J Appl Phys 2003;93:6252–6257.

104. Glass R, Arnold M, Cavalcanti-Adam EA, Blummel J, Haferkemper C, Dodd C, Spatz JP. Block copolymer micelle nanolithography on non-conductive substrates. New J Phys 2004;6:1–17.

105. Sniadecki N, Desai RA, Ruiz SA, Chen CS. Nanotechnology for cell-substrate interactions. Ann Biomed Eng 2006;34:59–74.

106. Blattler T, Huwiler C, Ochsner M, Stadler B, Solak H, Voros J, Grandin HM. Nanopatterns with biological functions. J Nanoscience Nanotechnol 2006;6:2237–2264.

107. Christman KL, Enriquez-Rios VD, Maynard HD. Nanopatterning proteins and peptides. Soft Matter 2006;2:928–939.

108. Falconnet D, Pasqui D, Park S, Eckert R, Schift H, Gobrecht J, Barbucci R, Textor M. A novel approach to produce protein nanopatterns by combining nanoimprint lithography and molecular self-assembly. Nano Lett 2004;4:1909–1914.

109. Falconnet D, Koenig A, Assi T, Textor M. A combined photolithographic and molecular-assembly approach to produce functional micropatterns for applications in the biosciences. Adv Funct Mater 2004;14:749–756.

110. Bae C, Shin HJ, Moon J, Sung MM. Contact area lithography (CAL): A new approach to direct formation of nanometric chemical patterns. Chem Mater 2006;18:1085–1088.

111. Valsesia A, Colpo P, Meziani T, Bretagnol F, Lejeune M, Rossi F, Bouma A, Garcia-Parajo M. Selective immobilization of protein clusters on polymeric nanocraters. Adv Funct Mater 2006;16:1242–1246.

112. Keselowsky BG, Collard DM, Garcia AJ. Surface chemistry modulates fibronectin conformation and directs integrin binding and specificity to control cell adhesion. J Biomed Mater Res A 2003;66:247–259.

113. Keselowsky BG, Collard DM, Garcia AJ. Surface chemistry modulates focal adhesion composition and signaling through changes in integrin binding. Biomaterials 2004;25:5947–5954.

114. Warchol ME. Cell density and N-cadherin interactions regulate cell proliferation in the sensory epithelia of the inner ear. J Neurosci 2002;22:2607–2616.

115. Schwarz US, Balaban NQ, Riveline D, Addadi L, Bershadsky A, Safran SA, Geiger B. Measurement of cellular forces at focal adhesions using elastic micro-patterned substrates. Mater Sci Eng C 2003;23:387–394.

116. Balaban NQ, Schwarz US, Riveline D, Goichberg P, Tzur G, Sabanay I, Mahalu D, Safran S, Bershadsky A, Addadi L, et al. Force and focal adhesion assembly: A close relationship studied using elastic micropatterned substrates. Nat Cell Biol 2001;3:466–472.

117. Beningo KA, Dembo M, Kaverina I, Small JV, Wang YL. Nascent focal adhesions are responsible for the generation of strong propulsive forces in migrating fibroblasts. J Cell Biol 2001;153:881–887.

118. Tolic-Norrelykke IM, Wang N. Traction in smooth muscle cells varies with cell spreading. J Biomech 2005;38:1405–1412.

119. Franz CM, Muller DJ. Analyzing focal adhesion structure by atomic force microscopy. J Cell Sci 2005;118:5315–5323.

120. Engler AJ, Sen S, Sweeney HL, Discher DE. Matrix elasticity directs stem cell lineage specification. Cell 2006;126:677–689.